nuclear fusion
IAEA

PAPER • OPEN ACCESS

3D radiated power analysis of JET SPI discharges using the Emis3D forward modeling tool

To cite this article: B. Stein-Lubrano *et al* 2024 *Nucl. Fusion* **64** 036020

View the article online for updates and enhancements.

You may also like

- 3D radiation, density, and MHD structures following neon shattered pellet injection into stable DIII-D Super H-mode discharges
R. Sweeney, L.R. Baylor, N.W. Eidietis et al.
- Operational issues at high lower hybrid power density in JET: waveguide conditioning and arc detection
M Goniche, J Mailloux, I Coffey et al.
- Interpretive modelling of boron transport in the boundary plasma of WEST experiments with the impurity powder dropper
K. Afonin, A. Gallo, Y. Marandet et al.

This content was downloaded from IP address 18.29.15.223 on 30/05/2024 at 18:21

OPEN ACCESS
IOP Publishing | International Atomic Energy Agency
Nuclear Fusion
Nucl. Fusion **64** (2024) 036020 (21pp)
https://doi.org/10.1088/1741-4326/ad1d10

3D radiated power analysis of JET SPI discharges using the Emis3D forward modeling tool

B. Stein-Lubrano[1,*], R. Sweeney[1,a], D. Bonfiglio[2,3], J. Lovell[4], P. Carvalho[5], L. Baylor[4], R.S. Granetz[1], S. Jachmich[6], E. Joffrin[7], M. Kong[5,b], M. Lehnen[6], C. Maggi[5], E. Marmar[1], E. Nardon[7], P. Puglia[5], U. Sheikh[8], D. Shiraki[4], S. Silburn[5] and JET Contributors[c]

[1] Plasma Science and Fusion Center, MIT, Cambridge, MA 02139, United States of America
[2] Consorzio RFX, CNR, ENEA, INFN, Università di Padova, Acciaierie Venete SpA, C.so Stati Uniti 4, 35127 Padova, Italy
[3] CNR-ISTP, Padova, Italy
[4] Oak Ridge National Laboratory, Oak Ridge, TN 37831, United States of America
[5] United Kingdom Atomic Energy Authority, Culham Centre for Fusion Energy, Culham Science Centre, Abingdon, Oxon OX14 3DB, United Kingdom of Great Britain and Northern Ireland
[6] ITER Organization, Route de Vinon sur Verdon, 13115 St Paul Lez Durance, France
[7] CEA, IRFM, F-13108 Saint-Paul-lez-Durance, France
[8] École Polytechnique Fédérale de Lausanne (EPFL), Swiss Plasma Center (SPC), Lausanne CH-1015, Switzerland

E-mail: bsteinlu@mit.edu

Received 26 June 2023, revised 16 October 2023
Accepted for publication 10 January 2024
Published 9 February 2024

Abstract

Precise values for radiated energy in tokamak disruption experiments are needed to validate disruption mitigation techniques for burning plasma tokamaks like ITER and SPARC. Control room analysis of radiated power (P_{rad}) on JET assumes axisymmetry, since fitting 3D radiation structures with limited bolometry coverage is an under-determined problem. In mitigated disruptions, radiation is toroidally asymmetric and 3D, due to fast-growing 3D MHD modes and localized impurity sources. To address this problem, Emis3D adopts a physics motivated forward modeling ('guess and check') approach, comparing experimental bolometry data to synthetic data from user-defined radiation structures. Synthetic structures are observed with the Cherab modeling framework and a best fit chosen using a reduced χ^2 statistic. 2D tomographic inversion models are tested, as well as helical flux tubes and 3D MHD simulated structures from JOREK. Two nominally identical pure neon shattered pellet injection (SPI) mitigated discharges in JET are analyzed. 2D tomographic inversions with added toroidal freedom are the best fits in

[a] Present affiliation Commonwealth Fusion Systems, Devens, MA 01434, United States of America.
[b] Present affiliation École Polytechnique Fédérale de Lausanne (EPFL), Swiss Plasma Center (SPC), Lausanne CH-1015, Switzerland.
[c] See Mailloux *et al* 2022 (https://doi.org/10.1088/1741-4326/ac47b4) for JET Contributors.
[*] Author to whom any correspondence should be addressed.

Original Content from this work may be used under the terms of the Creative Commons Attribution 4.0 licence. Any further distribution of this work must maintain attribution to the author(s) and the title of the work, journal citation and DOI.

© 2024 The Author(s). Published by IOP Publishing Ltd on behalf of the IAEA. All rights reserved

the thermal quench (TQ) and current quench (CQ). In the pre-TQ, 2D reconstructions are statistically the best fits, but are likely over-optimized and do not capture the 3D radiation structure seen in fast camera images. The next-best pre-TQ fits are helical structures that extend towards the high-field side, consistent with an impurity flow under the magnetic nozzle effect also observed in JOREK simulations. Whole-disruption radiated fractions of $0.98 + 0.03/-0.29$ and $1.01 + 0.02/-0.17$ are found, suggesting that the stored energy may have been fully mitigated by each SPI, although mitigation efficiencies well below ITER and SPARC requirements for high energy pulses are still within the large uncertainties. Emis3D is also used to validate JOREK SPI simulations, and confirms improvements in matching experiment from changes to impurity modeling. Time-dependent toroidal peaking factors are calculated and discussed.

Keywords: disruption, tokamak, mitigation, shattered pellet injection, bolometry, Cherab, JET

(Some figures may appear in colour only in the online journal)

1. Introduction

Two new tokamak experiments, ITER [1] and SPARC [2], are currently under construction with the goal of achieving fusion gain Q well in excess of unity, also referred to as 'breakeven'. To achieve breakeven, these machines will reach higher plasma temperatures and comparable or higher densities to present day experiments, and consequently higher stored energies. The increase in stored energy comes with increased risk of damage to the machine, especially during major disruption events. In these events, stored energy is rapidly released and can cause mechanical and melt damage to divertors and other plasma facing components (PFCs) [3].

Disruption damage can be prevented or minimized through use of a disruption mitigation system (DMS) that rapidly injects large quantities of impurities into the plasma [4]. In ITER, impurities will be delivered through shattered pellet injection (SPI) [5], and in SPARC, impurities will be delivered by massive gas injection (MGI) [6]. The goal of impurity injections is to radiate the stored energy isotropically, leaving less energy deposited in localized regions of the divertor or PFCs. Successful mitigation requires high radiated energy fractions $f_{\mathrm{rad}} = W_{\mathrm{rad}}/W_{\mathrm{stored}}$, where W_{rad} is the radiated energy and W_{stored} is the sum of the plasma thermal energy W_{th} and magnetic energy W_{mag}, minus the magnetic energy coupled to conductors [7]. For high-performance discharges on ITER, the radiated fraction of the stored thermal energy $f_{\mathrm{rad,th}} = W_{\mathrm{rad,th}}/W_{\mathrm{th}}$ must be at least 90% to ensure the divertor is not damaged [8], and similar limits are expected on SPARC. Similarly successful radiation of W_{mag} is also desired. To investigate whether the ITER DMS design will reliably achieve high f_{rad}, several mitigation experiments have been conducted on JET [5, 9–11]. The radiated fractions calculated from these experiments have large uncertainties due to limitations in bolometry diagnostics and analysis methods available on JET, leaving the validation of achieving 90% an open question [12, 13].

Measuring f_{rad} in disruption studies has unique challenges. Space for bolometry diagnostics is limited, and diagnostics are often optimized for performance during flattop. Flattop radiation is generally toroidally symmetric, with radiation distributions that are relatively stable in time. For stable, toroidally symmetric radiation structures, P_{rad} can be accurately approximated using a bolometer array at a single toroidal location by a weighted sum of bolometer channel brightnesses. In major disruptions, by contrast, radiation structures evolve rapidly, and toroidal symmetry is broken by tearing modes, localized impurities, and three-dimensional heat fluxes [10, 14, 15]. Toroidal asymmetry is seen in fast camera images of visible radiation such as figure 1 [16]. A single bolometer array does not accurately capture three dimensional radiation structures, leading to large uncertainties in P_{rad} and f_{rad} [12].

To better capture 3D radiation structures, a 3D 'feed-forward tomography' code called Emis3D is developed [17, 18]. Emis3D uses reduced χ^2 goodness-of-fit testing to select a best fit radiation structure from a large library of user-provided radiation structure options. The additional constraints introduced by the user-provided radiation structures overcome the highly under-determined problem that challenges standard tomography techniques.

The best fit structure should not be interpreted as a precise match to the true radiation structure, but rather it serves as a selection tool for comparing different physical models of possible radiation and plasma behavior. Careful interpretation of best- and close-fit radiation structures can yield insights into plasma and radiation behaviors that are not provided by a weighted sum P_{rad} calculation alone.

Overcoming the under-determined problem comes with a cost; the Emis3D approach introduces human bias by relying on a user-provided pool of radiation structures and fitting parameter choices. To minimize this error, our radiation structure choices are informed in part by observations from fast camera images, simulations, and by previous works [15, 16]. Three-dimenionsal structures derived from 2D tomographic inversions are included in the pool when appropriate. A range of possible results based on different physical and fitting assumptions are presented here to demonstrate the freedom in the fitting process and the degeneracy inherent in this under-determined problem.

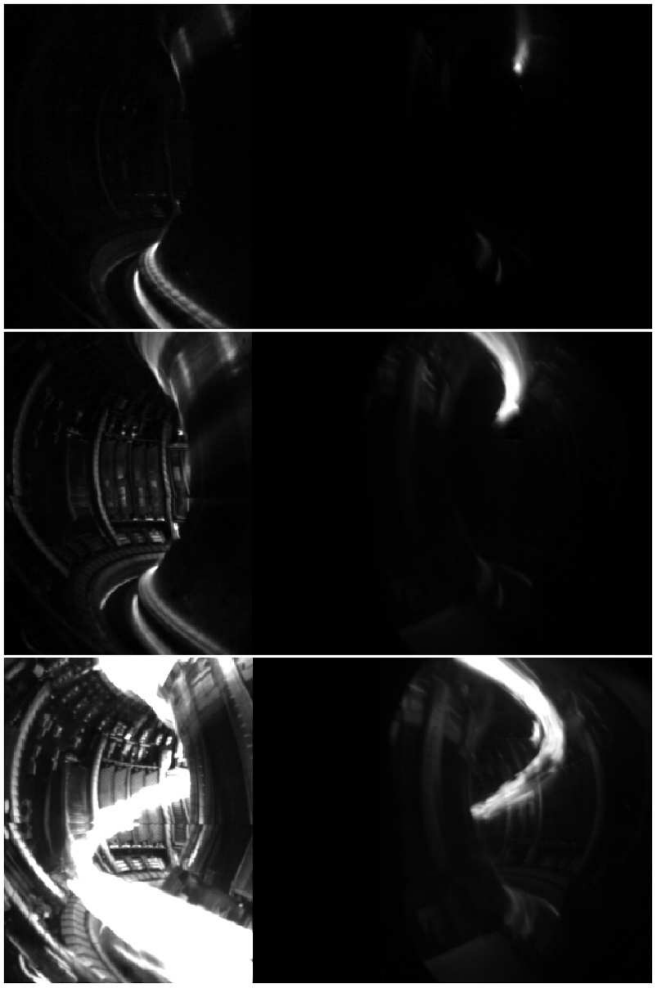

Figure 1. Fast camera images from the pre-TQ of a JET SPI discharge showing toroidally asymmetric helical flux tube radiation structures. All three images are from shot number 96 874, a deuterium pellet SPI injection. Top images are from just after the injection, time 9.0 430, and show a small bright spot where pellet shards have begun to ablate. Middle images are from the very early pre-TQ, time 9.0 446, and show a helical structure. This helical structure extends mostly in the direction of the high-field side from the injection location (clockwise, as seen from above). Bottom images are from later in the pre-TQ, time 9.0 458, and show another helical structure, this one extending in both directions from the injection location. The left images are unfiltered; the right images are filtered to deuterium alpha wavelength 656.1 nm.

As a demonstration of the capabilities of Emis3D, we investigate two SPI disruptions from the 2019-2020 JET SPI campaign. JET discharge number 95 709 has relatively low peak P_{rad} according to weighted sum P_{rad} calculations, while discharge 95 711 has relatively high peak P_{rad}, suggesting relatively low and high $f_{\mathrm{rad,\,th}}$, respectively. We will refer to these discharges as 'low $f_{\mathrm{rad,\,th}}$' and 'high $f_{\mathrm{rad,\,th}}$', or just as 'low f_{rad}' and 'high f_{rad}'. These disruptions are of particular interest because the plasma and injected pellet were identically prepared. Using Emis3D, we investigate possible radiation structures, radiated powers, and toroidal peaking factors (TPFs) throughout these two disruptions and propose a hypothesis for the apparent difference in f_{rad} between these nominally identical shots. The TPF of a radiation structure is defined as

$$\mathrm{TPF} = \frac{\max\left(\mathrm{d}P_{\mathrm{rad}}/\mathrm{d}\phi\right)}{\mathrm{mean}\left(\mathrm{d}P_{\mathrm{rad}}/\mathrm{d}\phi\right)}$$

$$P_{\mathrm{rad}} = \int \mathrm{d}V\,\epsilon = \int r\mathrm{d}A \int \mathrm{d}\phi\;\epsilon$$

$$\left.\frac{\mathrm{d}P_{\mathrm{rad}}}{\mathrm{d}\phi}\right]_{\phi_0} = \int r\;\mathrm{d}A\;\epsilon(r,\theta,\phi_0)$$

where $\epsilon(r,\theta,\phi)$ is the plasma emissivity as a function of position, ϕ is the toroidal angle, the integrals over V and A are over the total plasma volume and each ϕ_0 cross-section respectively, and $\mathrm{d}P_{\mathrm{rad}}/\mathrm{d}\phi]_{\phi_0}$ is the contribution of the ϕ_0 cross-section to P_{rad}. TPF is a convenient measure of toroidal asymmetry, although it does not fully capture asymmetry in the distribution of radiation sources across different poloidal cross-sections.

In section 2 the JET bolometry systems are described. In section 3 the two nominally identical discharges are described. In section 4 the Emis3D forward modeling approach is described. In section 5, the deuterium injection from figure 1 is revisited, and an adjustment is made to the Emis3D radiation structure library to better match the evidence from fast camera images. In section 6 the forward modeling results for the two discharges are described. In section 7 an additional application of Emis3D for validation of nonlinear 3D MHD simulations with the JOREK code is presented. Final remarks and conclusions are drawn in section 8.

2. JET bolometry

As of the 2019 JET SPI campaign, JET has two foil bolometer arrays for radiated power analysis: a vertical array at the top of the machine looking downwards towards the divertor, and a horizontal array on the outboard side of the machine looking towards the inboard wall (figure 2). Each of the two large arrays is composed of 24 individual bolometer channels, together covering an entire poloidal cross-section of the plasma, and the two arrays are toroidally located 135 degrees apart. These arrays have time resolutions on the order of 0.5–1 ms, roughly comparable to the thermal quench (TQ) timescale on JET. Control room P_{rad} measurements are made using the vertical bolometer array only.

JET also has four individual vertical foil bolometer channels located at four different toroidal locations, providing extra toroidal coverage. However, these channels have limited poloidal coverage and high background noise, which complicates analysis on fast disruption timescales. The individual channels are therefore not used in the radiation structure fitting. Their integrated signals over an entire disruption provide information on the average toroidal peaking, which will be compared with synthetic predictions from the fitted data in section 6.4.

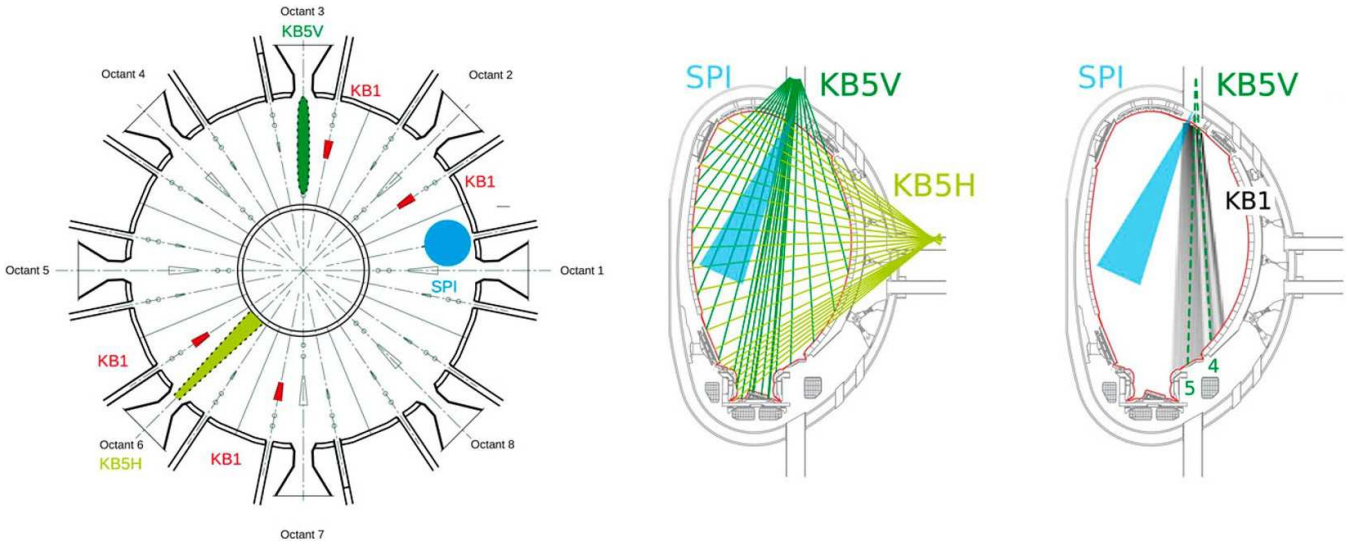

Figure 2. JET Bolometry available to 2019 SPI campaign. KB5V provides vertical sightlines of the plasma region in octant 3, with higher resolution in the divertor. KB5H provides horizontal sightlines in octant 6, likewise with higher resolution near the divertor. The four KB1 channels near octants 2, 3, 6, and 7 have sightlines through the plasma center and into the divertor. Reprinted from [12], with the permission of AIP Publishing.

3. Experimental setup

Two H-mode plasma discharges terminated by a shattered pellet injector (SPI) on the JET tokamak are studied here to understand the mitigation performance. These discharges use a moderate beam power of 15 MW and a modest ion-cyclotron resonant heating heating power of 2 MW, where the latter is to reduce impurity accumulation. These discharges reach peak thermal energies of near 4 MJ. After reaching flattop and allowing profiles to equilibrate, a dominantly neon pellet carrying 2.46×10^{22} atoms is fired into the stable discharge. Heating is turned off just prior to injection for machine protection, and thermal energy tapers to 3.5 MJ before the pellet reaches the plasma. Relevant pellet properties and plasma parameters at the time of arrival of the shattered impurity are reported in table 1 and figure 3.

As the impurity arrives it is observed on a fast eXtreme UltraViolet (XUV) diamond detector [19], and on a D-alpha filterscope. The XUV detector is displaced toroidally from the injection and therefore this signal is delayed by the toroidal transit time of the impurities. The D-alpha filterscope view is near the injection location and it observes both radiation from deuterium injected in the shattered material as well as edge plasma deuterium that is quickly cooled by dilution and impurity radiation. The flight time of the pellet is a useful way to diagnose any irregularities in the injection process and is defined as the XUV detector rise time minus the microwave cavity peak time. The microwave cavity diagnostic is a resonant microwave chamber that the pellet passes through, allowing a measurement of the pellet mass [20]. Velocity of the pellet can also be derived directly from this diagnostic alone, but this technique is not used here. The microwave cavity data for these two discharges confirm that both injections were a single pellet with comparable mass prior to shattering.

Table 1. Discharge parameters and pellet properties for the identically prepared SPIs. The pellets are pure cryogenic neon with a deuterium shell. The D2 quantities listed are in the pellet shell and do not include propellant D2 atoms. W_{th} and W_{mag} are as defined in [7]. n_e and T_e are measured by Thompson scattering. f_{rad} and P_{rad} are as determined by the JET control room vertical bolometer weighted average, known as 'TOPI' [21].

Discharge label	'low f_{rad}'	'high f_{rad}'
JET Shot Number	95 709	95 711
I_p (MA)	2.5	2.5
B_T (T)	2.5	2.5
W_{th} (MJ)	3.5	3.6
W_{mag} (MJ)	8.0	8.1
n_e (m^{-3})	7.24	7.25
T_e (keV)	2.89	2.95
Ne Content (atoms)	$2.46{\cdot}10^{22}$	$2.46{\cdot}10^{22}$
D2 Content (atoms)	$5.74{\cdot}10^{21}$	$5.74{\cdot}10^{21}$
Ne Fraction	0.81	0.81
Propellant Species	D2	D2
Pellet Flight time (ms)	35.8	34.4
f_{rad}	0.80	0.90
Peak P_{rad} (GW)	2.12	4.74

The injected impurity causes a plasma disruption, which is subdivided in three general stages. In the pre-TQ, the injected impurity begins to radiate energy from the plasma, and P_{rad} increases. In the TQ, core confinement drops and most of the plasma's stored thermal energy is rapidly released, either as radiation or into the divertor. The TQ definition used in this paper is simply the 500 μs timestep in which the peak P_{rad} occurs. The current quench (CQ) refers to the period immediately after the TQ and lasting until the complete loss of plasma, in which the plasma's stored magnetic energy is more slowly released, either into electrically conducting plasma

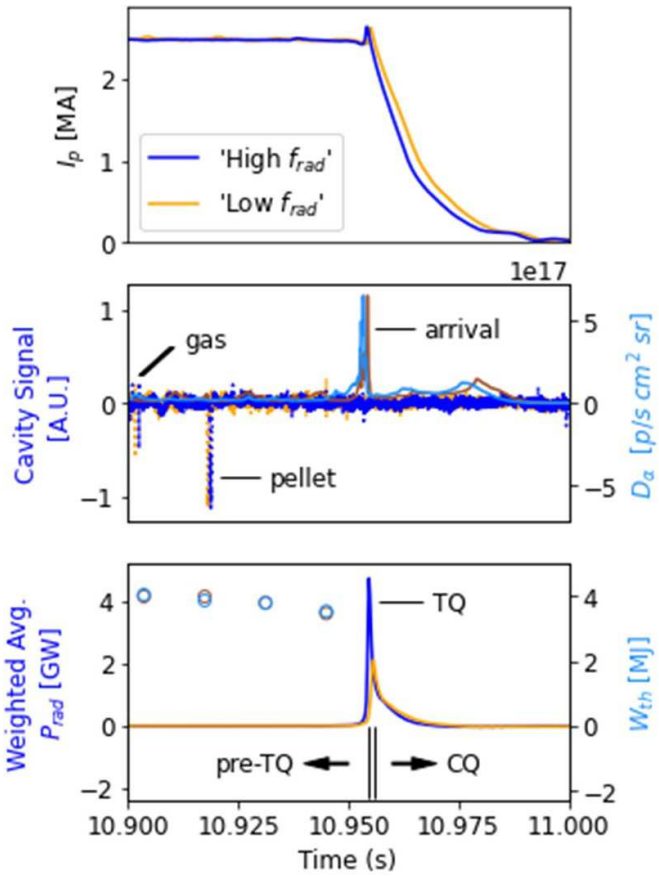

Figure 3. General shot parameters for the 'high' and 'low f_{rad}' discharge disruptions. Propellant gas is detected moving through the microwave cavity, followed by the cryogenic pellet. Impurity arrival in the plasma is detected by the D-alpha filterscope, after which radiated power increases sharply and plasma current begins to decrease. The two discharges are nearly identical except for the large difference in observed TQ P_{rad}.

facing components and the vacuum vessel, or through conversion to thermal energy and subsequent radiation and parallel transport into the wall.

Control room analysis using a radiated power derived from a weighted sum of the vertical bolometer channels suggests a more than factor of two difference in the peak radiated power between these otherwise identical discharges. Repeatability of these JET experiments is crucial to demonstrate reliability of SPI for ITER, and therefore these two discharges serve to both address this concern and to provide a manageable data set for the first detailed analysis using the Emis3D code.

4. Emis3D

4.1. Overview

Emis3D calculates W_{rad} for a single disruption by identifying best-fit radiation structures at each timestep and integrating their radiated powers. The best fit radiation structures are selected from a library of radiation structure options, which are synthetically 'observed' in advance by the synthetic diagnostic framework Cherab [22, 23]. Synthetically 'observing' a radiation structure yields a fingerprint of bolometer channel brightnesses that is compared at each timestep to experimental bolometer brightnesses through reduced χ^2 goodness-of-fit testing. The best-fit radiation structure at each timestep is identified in three stages: first optimization of each radiation structure option, then selection of the best fit radiation structure, and finally toroidal distribution selection. See figure 4 for a diagram of the Emis3D algorithm.

In the optimization stage, each radiation structure in the library is optimized to fit the experimental data at that timestep as closely as possible (minimizing χ^2), within the constraints of the radiation structure definition. In accordance with the forward modeling approach, each radiation structure option is highly constrained, and only slight optimization is possible. For a given toroidally self-similar structure, the only degree of freedom is the amplitude of the radiation structure. There are two amplitude parameters for these radiation structures, one fitted to the vertical bolometer array, and one to the horizontal array. For the toroidally asymmetric 'helical' radiation structures introduced in the next section, there are two additional amplitude parameters, corresponding to second 'punctures' of the radiation structure through the plane of each

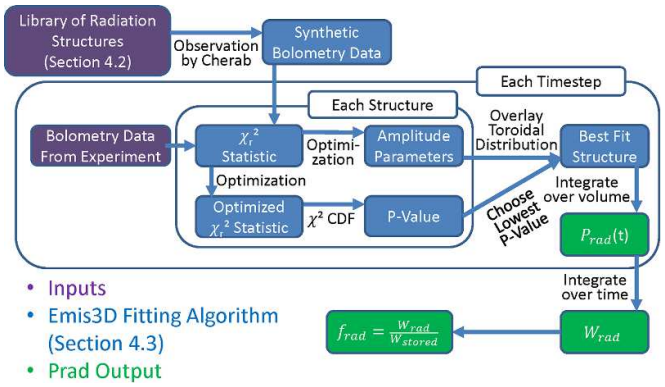

Figure 4. A flowchart diagram of the Emis3D algorithm.

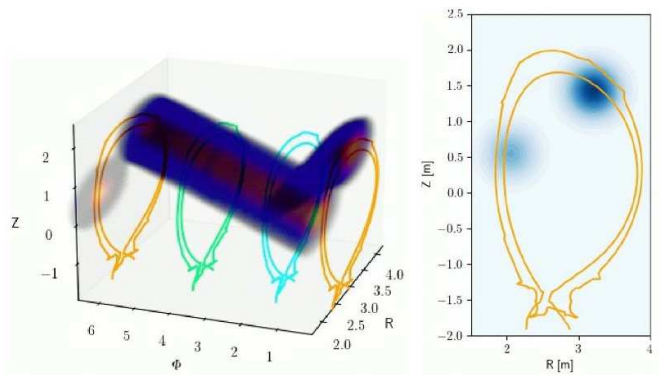

Figure 5. An example helical radiation structure following more than one toroidal revolution of a field line and leaving multiple 'punctures' through poloidal cross-sections. The unwrapped plot (left) shows the radiation pattern in purple, and outlines of the first wall and pre-disruption last closed flux surface are shown in the planes of the SPI injection (orange), the vertical bolometer array (blue), and the horizontal bolometer array (green). The right plot shows the two-spot radiation pattern of this helical structure in the plane of the injector.

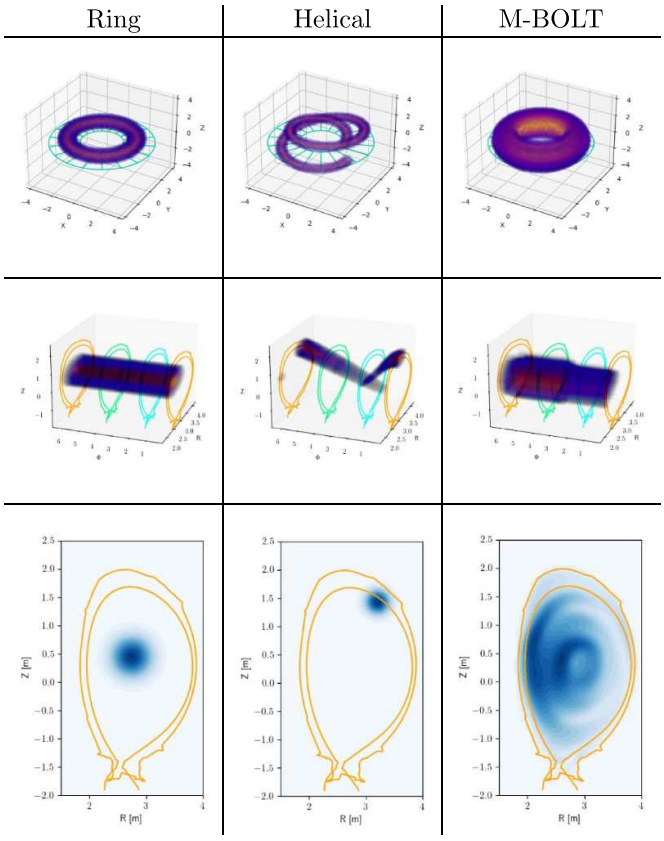

Figure 6. Examples of the radiation structure classes included in the radiation structure library. Top are wrapped bubble plots, showing the radiation structure as it might look in real space from an outside perspective with no obstruction from the tokamak. No toroidal distribution is applied in the top figures. Middle are unwrapped bubble plots of the same radiation structures, with the toroidal ϕ dimension unwrapped to a linear dimension. Example toroidal distributions are applied to the unwrapped plots: An asymmetric gaussian in ϕ is applied to the helical, and a step function in ϕ is applied to the M-BOLT. Bottom are cross-sections of these structures in the $\phi = 0$ (near injector) plane.

bolometer array, as the helical structure is followed up to two toroidal revolutions. An example of double punctures is shown in figure 5. These amplitude parameters are later used in the third stage of determining the toroidal distribution of the radiation structure.

In the selection stage, the reduced χ^2 of the optimized radiation structures are compared, and the best fit radiation structure chosen. This stage is described in section 4.3.

Up to this point, the amplitude of the chosen radiation structure is known only at the locations of the two bolometer arrays. In the toroidal distribution selection stage, the amplitudes found in the optimization stage are used to constrain a toroidal distribution for the radiation structure. Various toroidal distributions derived from different physical models will be tested and the results compared.

Absolute calibration of radiation structures is demonstrated by close agreement between experimental bolometry data and Cherab synthetic bolometry data of 2D tomographically reconstructed BOLT radiation structures. For more on absolute calibration, see the appendix.

4.2. Radiation structure library

Each radiation structure object in Emis3D consists of a 3D function of emissivity, synthetic bolometry data for that emissivity function, and the total radiated power produced by that function when integrated over the plasma volume. The toroidal dependence of the candidate distribution is not set in advance; the integrated radiated power is binned in 18 toroidal sections, to allow fitting a toroidal dependence in the toroidal distribution selection stage. Radiation structures are referred to here as 'toroidally self-similar' if their cross-sectional radiation source distribution is the same at all toroidal angles, with variation only in total cross-section amplitude. Radiation structures with no toroidal symmetry are referred to as 'toroidally asymmetric'.

Three general classes of radiation structure are used, and are now discussed. Examples of each radiation structure type are displayed in figure 6 for reference. A fourth class of radiation distributions, derived from JOREK simulations, are not

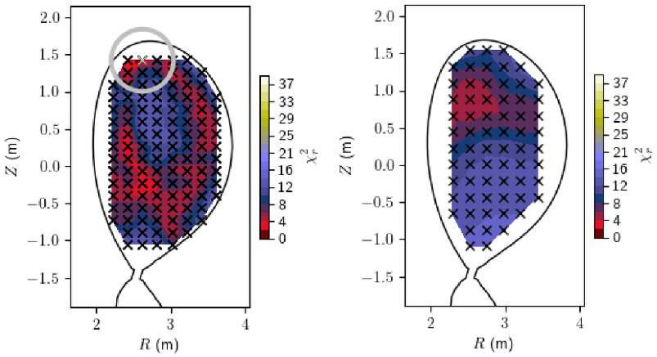

Figure 7. Example arrays of helical and ring structures represented by their R and Z center locations marked with an x, and colored by their quality of fit to experimental data. Helical centers correspond to their R and Z centers at $\phi = 0$, near the plane of the SPI injector. These reduced χ^2 are from the late pre-TQ of the 'low f_{rad}' disruption, at time 10.954 s. The best fit helical at this time is marked and circled in grey.

included in the main radiation library, but will be discussed in section 7.

'Ring' structures are toroidally self-similar. Their poloidal cross-sections are circular, centered on some major radius R and vertical coordinate Z, with a bivariate Gaussian distribution in both R and Z around that point. We include a collection of ring distributions of the same 0.25cm Gaussian width, but centered at different R and Z locations, in our candidate pool, as seen in figure 7. The R and Z locations are taken from a regular grid within the last closed flux surface of the pre-disruption plasma.

'Helical' structures represent concentrated impurity radiation from a flux tube centered around a pre-disruption magnetic field line. Like ring structures, they have a circular Gaussian poloidal cross-section, but unlike rings, they are not toroidally self-similar. The R and Z center of the Gaussian cross-section instead follows a field line around the torus up to two revolutions, one in each direction from the injector location. These distributions are inspired by fast camera images from SPI disruptions that show visible radiation following field lines during the pre-TQ, as seen in figure 1, as well as previous works that suggest the disruption radiation is field aligned [15, 16]. As with rings, collections of helicals starting from a similar R and Z grid are included in the candidate pool. We include three collections with different gaussian widths: 0.15 cm, 0.25 cm, and 0.35 cm.

Modified-BOLometer Tomography (M-BOLT) structures are the standard JET BOLT tomographic reconstructions produced upon request, with the modification of the toroidal distribution overlay described in section 4.4. The BOLT process uses lagrangian optimization to generate a two dimensional radiation distribution from vertical and horizontal bolometer array data [24, 25]. Radiation sources are constrained and smoothed along flux surfaces. Toroidal self-similarity is assumed. If there is a large difference in signal magnitudes between the two bolometer arrays, the horizontal array is manually scaled to the vertical array prior to optimization. Note that the scaling process of section 4.4 is done by reduced χ^2 fitting, so the final radiation structure amplitude is not subject to direct human input. We have included M-BOLT structures at approximately 1 ms intervals throughout both disruptions.

A second set of 2D tomographic reconstructions are available for these discharges, automatically produced using neural networks [26]. However, the neural networks for these reconstructions are designed for and trained on entire JET discharges, rather than specifically disruption bolometry data, and can produce unusual results when applied to disruptions. These reconstructions are not included in the Emis3D radiation structure library.

4.3. Fitting

The library of radiation structures and their synthetic bolometer measurements are compared to experimental data from both bolometer arrays at each timestep. The radiation structure library is not varied from timestep to timestep; all distributions are available at all timesteps. For example, M-BOLT structures derived from CQ data are not strictly limited to the CQ; they are available as candidates for the radiation structure during the pre-TQ as well, but are not typically close fits.

The goodness of fit between the array of synthetic values $[C_i]$ observed for a given structure and the array of bolometer data $[O_i]$ at a given timestep is quantified using a reduced χ^2 statistic:

$$\chi^2_\nu = \frac{1}{\nu}\sum_i \frac{(O_i - C_i)^2}{\sigma_i^2} \qquad \nu = N - f - 1$$

where σ_i are the standard errors of each bolometer channel, ν is the degree of freedom, N is the number of bolometer channels, and f is the number of fitted parameters. The vertical and horizontal bolometer arrays both have 24 channels, but one faulty vertical bolometer channel is excluded from the fitting process, so $N = 47$. Helical structures have four amplitude parameters, while ring and M-BOLT structures only have two. Therefore, $\nu = 42$ for helical distributions and $\nu = 44$ for rings and M-BOLTs. Reduced χ^2 is selected for its ease of computation, its known relationship to p-value, and its general insensitivity to the choice of bolometer errors.

The bolometer errors σ_i are not rigorously calculated but are rather assumed to be 10% of the maximum channel brightness at each time, based on recommendations from diagnosticians. 10% is the approximate magnitude of channel errors during flattop operation. Rigorous determination of σ_i during disruptions is complicated by the likely presence of additional error sources not present during flattop. Fortunately, the magnitude of σ_i is not greatly impactful in the selection of a best fit via reduced χ^2 fitting: scaling all σ_i uniformly amounts to only a uniform scaling of χ^2 across all candidates, and the best fit

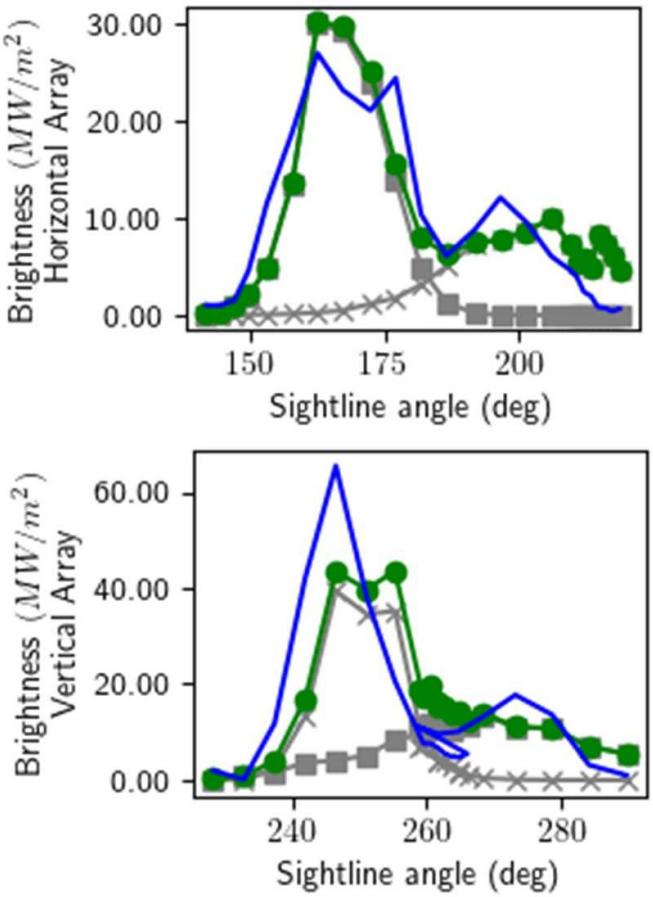

Figure 8. An example of synthetic bolometer channel brightnesses fitted to experimental bolometer data. Experimental bolometer channel brightnesses are in blue. Synthetic brightnesses from a best fit helical radiation structure are in green. The contribution from the first puncture is shown in grey squares, while the second puncture contribution is shown in grey $x - s$. Each contribution is scaled separately on each array in the optimization step, to produce the best combined match to the experimental data. This data is from the late pre-TQ of the 'low f_{rad}' disruption, at time 10.954 s, and the best fit helical structure in figure 7.

distribution remains the same. Only the uncertainties in values derived from radiation structures (P_{rad}, TPF) are affected.

The choice of flat 10% errors avoids overly weighting channels with low brightness, which are not as relevant to the total radiated power. This choice also allows variation in the magnitude of the σ_i from timestep to timestep. Scatter in the bolometer measurements suggest the error is proportional to the signal, however, a thorough investigation of the noise sources during disruptions has not been done.

The reduced χ^2 of each candidate is related to a p value through the reduced χ^2 cumulative distribution function:

$$p = 1 - \text{CDF}_\nu\left(\nu \cdot \chi^2_\nu\right)$$

[27]. The p value is a metric used in null hypothesis testing. The interpretation of a p value is delicate and should be carefully considered. In the χ^2 distribution case presented here, the null hypothesis is that the candidate radiation structure is exactly correct, and that measuring different $[O_i]$ values than $[C_i]$ is the result of the individual bolometer errors σ_i. The alternative hypothesis is that the candidate radiation structure is incorrect. The calculated p value is the probability that, when measuring N random variables, indexed by i, with expectation values C_i and standard errors σ_i, finding observations $[O_i]_{\text{test}}$ and an associated $(\chi^2)_{\text{test}}$, the resulting $(\chi^2)_{\text{test}}$ is greater than the χ^2 between $[O_i]$ and $[C_i]$.

If the p value is very small, then the likelihood of finding $[O_i]$ under the null hypothesis is very low. We then take the alternative hypothesis that the candidate source is incorrect and do not select it as the best fit. If the p value is high, then the observed $[O_i]$ could plausibly have been produced under the null hypothesis. This does not guarantee that the candidate distribution is correct, but it does mean that the distribution cannot be safely discarded. High p value candidates are therefore included in our pool of close fits, described in the following paragraph, with the highest p value (or lowest χ^2) as the best fit. Example synthetic bolometer data fitted to experimental data is shown in figure 8.

To provide error bars on the radiated power and peaking factors, a pool of close fits is considered in addition to the best fit. Because the σ_i used in this analysis are not directly associated with the true errors of each bolometer channel, and also

vary from timestep to timestep, the absolute p value found for each distribution is not reliable, and a fixed p value cutoff is not a good metric to define the pool of close fits. We instead define our close fit pool to include all structures up to two standard errors in p value below the best fit at each timestep, defined as $p_{\text{Cutoff}} = (1 - 0.9545) \cdot p_{\text{Best}}$ in accordance with the empirical rule (also known as the 68-95-99.7 rule). Because we do not have fully rigorous σ_i or an infinite library of radiation structures, the error bars derived using this approach cannot be interpreted as the true error in P_{rad} or TPF , but they are a useful metric for the variance in P_{rad} and TPF among the close fit radiation structures within the radiation structure library.

4.4. Toroidal distribution overlay

The ability to accommodate toroidal asymmetry is central to Emis3D. However, there is a very large domain of possible toroidal distributions an emissivity function could have, and data points from only two toroidal locations (the bolometer array locations) to constrain these distributions. Emis3D addresses this problem by isolating the choice of toroidal distribution from the rest of the fitting process. After a best fit distribution is selected, different toroidal distributions can be applied to the best fit distribution to test the effect of different physical models on P_{rad} and TPF.

Emis3D isolates the toroidal distribution of radiation structures by dividing each radiation distribution into toroidal bins. In this paper, the tokamak is divided into 18 bins of 20 degrees each. In the Cherab observation stage, the radiated power of a given radiation structure emitted within each bin is calculated separately. After the radiation structure optimization stage, the fitted amplitudes of the radiation structure at each array location are used to optimize a toroidal distribution for that radiation structure. The Cherab binned radiated powers are multiplied by the magnitude of the toroidal distribution at each toroidal location and summed to give the total radiated power for the radiation structure. The functional form of the toroidal distribution is selected by the user. Different distributions, based on different physical models or intuitions, can be tested, and the results compared.

Figure 9 shows three choices of toroidal distribution for M-BOLT structures: a simple step function, where the amplitude of the radiation structure matches the amplitude parameter fitted to the nearest bolometer array; a sinusoidal distribution, peaked or anti-peaked at the SPI injector location; and a linear interpolation, which is functionally equivalent to the step function. The results of each case are explored in greater depth in sections 6.1 and 6.2. Only one toroidal distribution for helical radiation structures is explored in this paper: an asymmetric gaussian, peaked at the injector location, with different gaussian widths in the clockwise and counterclockwise directions. An example of this toroidal distribution shape is shown in figure 10. This choice of toroidal distribution is based on the assumption that in the pre-TQ stage of the disruption, which helicals are intended to describe, impurity density will be highest where the pellet shards are injected, and therefore

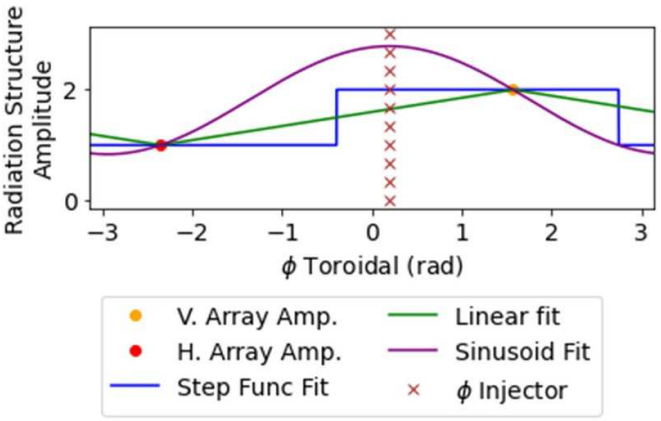

Figure 9. Three possible assumptions for the toroidal distribution of a M-BOLT radiation structure based on its amplitude at the vertical and horizontal array locations. The step function and linear fits are equivalent in terms of P_{rad} and TPF. The sinusoidal fit, in which radiation is assumed to peak at the injector location and spread smoothly in both directions, is not equivalent, and results in different P_{rad} and TPF. Note: this is a schematic for explanatory purposes and does not use data from any particular timestep.

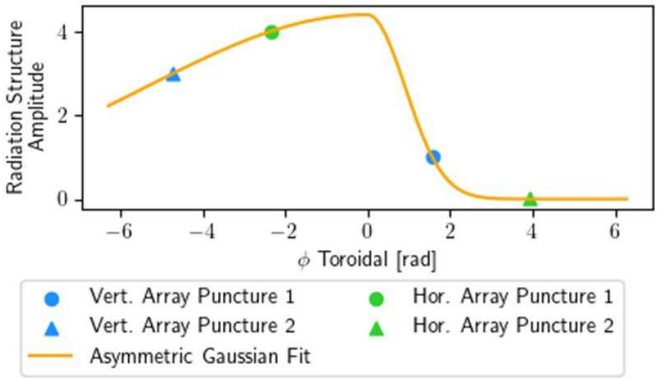

Figure 10. An example of an asymmetric Gaussian toroidal distribution for a helical radiation structure. The gaussian is peaked at the injector location, very close to zero radians. The amplitude of the function and the width of the Gaussian in each direction are fitted to the four amplitude fit parameters for a helical radiation structure. This toroidal distribution shows much higher radiation clockwise of the injector location, and implies preferred toroidal transport of impurities in that direction.

radiation will be peaked at the injector location. The impurities then ionize and are transported along field lines, but may transport at different rates in each direction, so the gaussian widths are fitted separately.

5. Deuterium injection

A pure deuterium SPI discharge (JET discharge 96 874) provides a discharge for study where the visible light structures observed by the fast camera are expected to well represent the dominant radiation structure measured by the bolometers. The 'low' and 'high f_{rad}' neon SPI discharges are not used

for this purpose because the neon injection radiation is mostly ultraviolet, not captured in visible fast camera images, and the fast cameras are further filtered to the neon-I wavelength on those discharges. Note that for high-Z injections the features observed in the fast cameras are not necessarily representative of the peak radiation features, as demonstrated on DIII-D [16]. In the deuterium SPI discharge, there is significant radiation in the visible spectrum, and the left and right fast cameras are unfiltered and deuterium-filtered, respectively. A pure deuterium pellet is used and clear helical structures are observed by the fast cameras throughout the pre-TQ, as shown in the top subpanel of figure 11.

This discharge is used as a test case to determine whether an M-BOLT structure or an Emis3D helical structure better represents the visible radiation during the pre-TQ. It is found that the M-BOLT fits the bolometer data better than the best fit helical, according to the Emis3D reduced χ^2 statistic and p-value testing. However, the Emis3D helical structure better captures the qualitative helical shape observed in the fast cameras. The best fit helical and the M-BOLT as observed by Cherab synthetic fast cameras are shown in the middle and bottom subpanels of figure 11 respectively, and can be compared to the experimental fast camera in the top subpanel. The nominally axisymmetric M-BOLT does not capture the helical structure. This demonstrates that using BOLT inversions during the pre-TQ could lead to incorrect conclusions about the 3D nature of the radiation.

M-BOLT structures are able to achieve better fits during the pre-TQ because the BOLT inversion process is both highly under-determined and well optimized, creating detailed, high resolution structures to precisely match the brightnesses of individual channels in the bolometer arrays. The BOLT inversions can result in unlikely anomalous radiation structure details like those shown in figure 12, although most cases are more subtle. The helical structures in this paper are not optimized to experimental data, except for amplitude scaling, and are therefore at a disadvantage to M-BOLTs for quality of fit. It may be possible in the future to account for this handicap by adjusting the degree of freedom ν used for M-BOLT structures in the reduced χ^2 formula to include constraints applied in the BOLT inversion process. Such an adjustment is not attempted here because it is non-trivial to interpret the BOLT optimization process as extra constraints in the context of ν.

There is additional support for favoring helical structures in the pre-TQ from the BOLT reconstructions themselves, from other experiments, and from JOREK simulations. In the pre-TQ BOLTs of the two disruptions investigated in this paper, there is a recurring double-spot radiation pattern highlighted in figure 12 that is consistent with radiation concentrations at different poloidal locations on each bolometer array, such as would result from a helical radiation structure. Similar patterns are observed in experiments on DIII-D [15] and KSTAR [28]. Further work at DIII-D has shown that the structures observed in the visible camera and the structures observed by the AXUV bolometers, while not consistent with each other, are both field aligned [16]. In JOREK simulations of JET SPI with plasma and pellet parameters equal to those of the two shots explored in this paper, there are helical radiation structures during the pre-TQ, as described in section 7 [29]. These simulated radiation structures produce a spectrum consistent with coronal equilibrium and the dominant power is not in visiblefrequencies. SPI simulations from DIII-D using NIMROD also show similar helical structures [30].

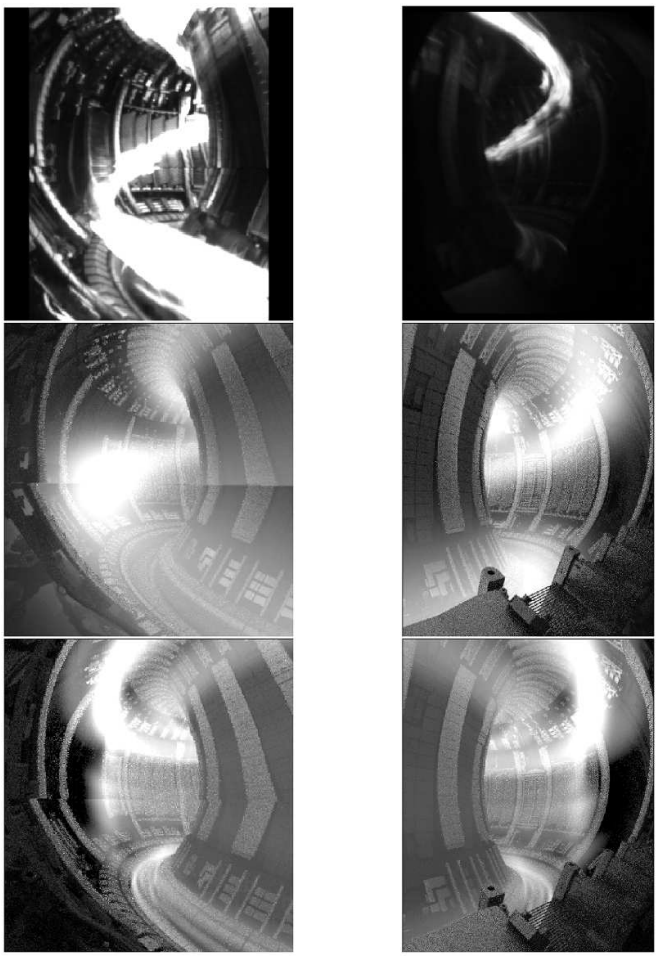

Figure 11. A comparison of best fit BOLT and helical radiation structures to fast camera images from a deuterium pellet SPI (JET shot number 96 874) in the pre-TQ. Top are visible range fast camera images from JET; left is unfiltered, right is filtered to show only the 656 nm Dalpha emission line. Middle are fully synthetic unfiltered fast camera images of the best fit helical distribution at this time, with a flat toroidal distribution, produced in Cherab using Raysect. Bottom are synthetic fast camera images of the best fit BOLT distribution at this time.

The combined evidence of these sources motivates our removal of M-BOLT structures derived from the pre-TQ from the Emis3D library, instead allowing helicals as the best fits during the pre-TQ. For completeness, multiple Emis3D reconstructions are performed for each discharge, and the case including pre-TQ M-BOLTs is also addressed. M-BOLTs are not removed from the TQ for lack of a preferred structure at this time, as TQ radiation structures are not well known, and expected to be more complicated than simple single helical shapes. This choice is revisited in section 6.3.

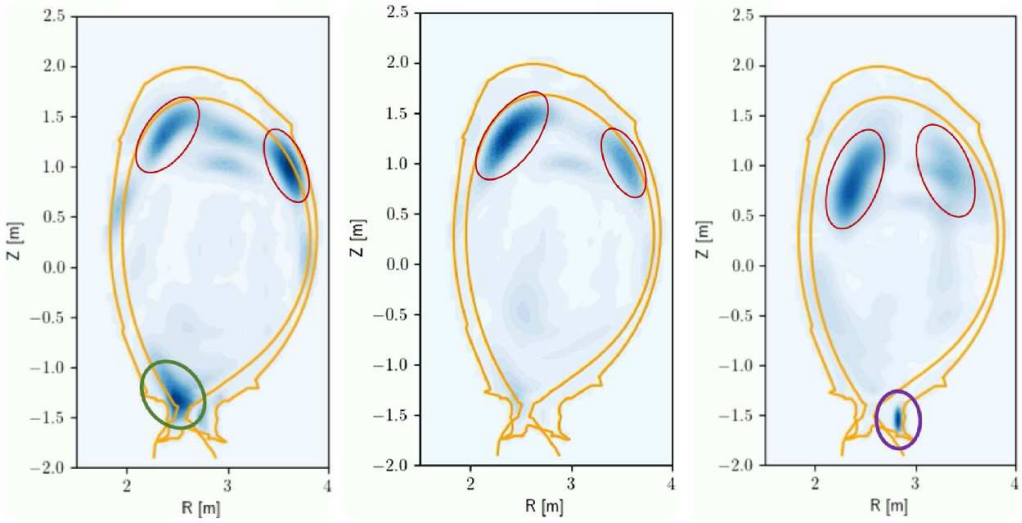

Figure 12. BOLT structure cross sections from the early (left), middle, and later (right) pre-TQ of the 'low $f_{\rm rad}$' disruption. The first wall and pre-disruption last closed flux surface are marked in yellow. The double radiation centers suggestive of a helical structure are circled in red. In the early pre-TQ, divertor-concentrated flattop radiation, circled in green, is a significant portion of overall radiation. Helical structures do not capture divertor radiation. By the middle pre-TQ, impurity radiation dominates and divertor radiation is not significant. The radiation spot circled in purple is a likely BOLT optimization anomaly. The radiation spot is outside the view of the horizontal bolometer array, so the BOLT algorithm may be using this radiation spot to fine-tune the fit to one or two vertical bolometer channels.

6. Results

Using the best-fit radiation structures chosen by the Emis3D algorithm for both the 'low $P_{\rm rad}$' and 'high $P_{\rm rad}$' disruptions, $P_{\rm rad}$ time series for each shot are reported in figures 13 and 14. Overall $f_{\rm rad}$ for the two disruptions are $0.98+0.03/-0.29$ and $1.01+0.02/-0.17$ respectively. The difference in $f_{\rm rad}$ between discharges is smaller than in the control room analysis, due to lower TQ radiation on the 'high $f_{\rm rad}$' discharge. Overall $f_{\rm rad}$ is higher than the control room result for both shots, due to higher radiated power in the early CQ. Both shots achieve $f_{\rm rad} > 0.9$, or $> 90\%$ of plasma energy radiated, which is considered successful mitigation. However, large lower uncertainties in the CQ mean that successful $> 90\% f_{\rm rad}$ mitigation cannot be guaranteed for either discharge. The small separation in $f_{\rm rad}$ between shots appears to be the result of toroidal peaking that was not captured by the control room analysis. Toroidal peaking factors (TPFs) for both shots are reported in figure 15.

Interpretation and modeling assumptions involved in these results are described in section 6.1. A variation in modeling of the toroidal distribution of M-BOLT radiation structures is considered in section 6.2. A case in which M-Bolts are removed from the TQ in addition to the pre-TQ is considered in section 6.3. Improvements in reproducing experimental single-channel bolometer brightnesses with the use of pre-TQ helical structures is presented in section 6.4.

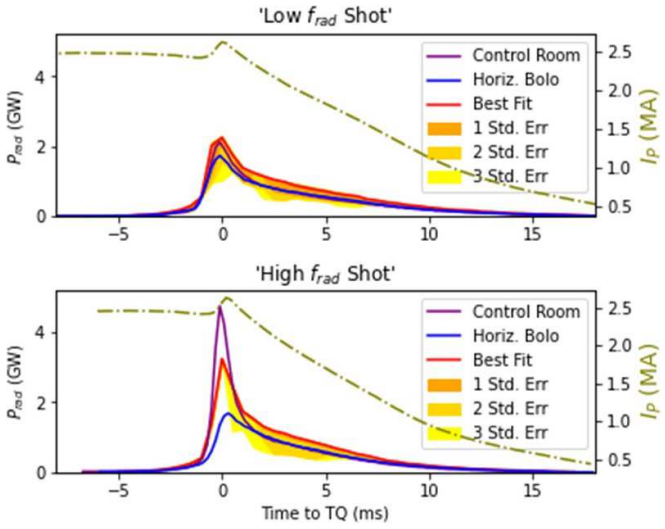

Figure 13. $P_{\rm rad}$ during the identically prepared 'low' and 'high' $f_{\rm rad}$ disruptions, with uncertainty bounds derived from the pool of close fits from the radiation structure library. The control room vertical bolometer-derived weighted average $P_{\rm rad}$, as well as a similar horizontal bolometer-derived weighted average, are included for reference. This horizontal bolometer weighted average is not a standard JET signal, but it has been referenced in previous publications [7, 31]. Emis3D finds lower $P_{\rm rad}$ at the thermal quench of the 'high $f_{\rm rad}$' discharge than the control room analysis. The timestep of peak $P_{\rm rad}$ is used interchangeably with 'thermal quench' in this paper.

6.1. Base Scenario

All helical and ring radiation structures are included in the radiation structure library, and M-BOLT radiation structures from either shot are included, from the time of the TQ through the end of the CQ. Pre-TQ M-BOLT structures are excluded, to favor helical structures as best fits in the pre-TQ, consistent with the conclusions of section 5. The exclusion of pre-TQ M-BOLTs has only a small effect on $f_{\rm rad}$, since pre-TQ radiation is low compared to the thermal and CQs. However, there is a large effect on toroidal peaking factors (figure 15), and the

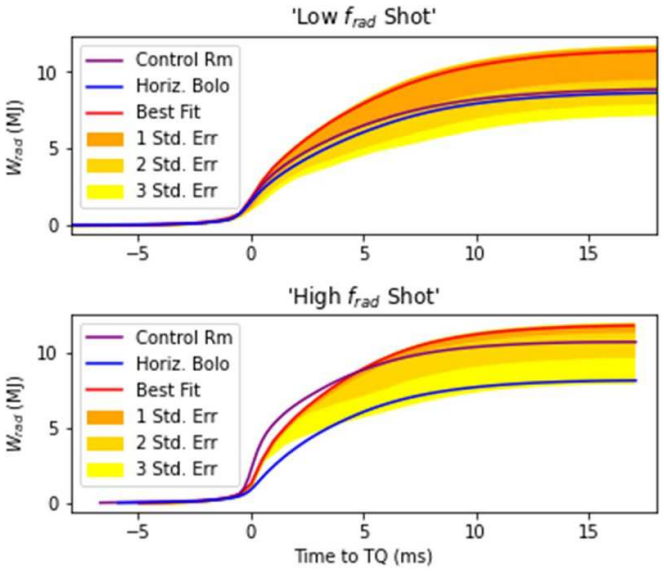

Figure 14. Cumulative W_{rad} from the identically prepared 'low' and 'high' f_{rad} disruptions.

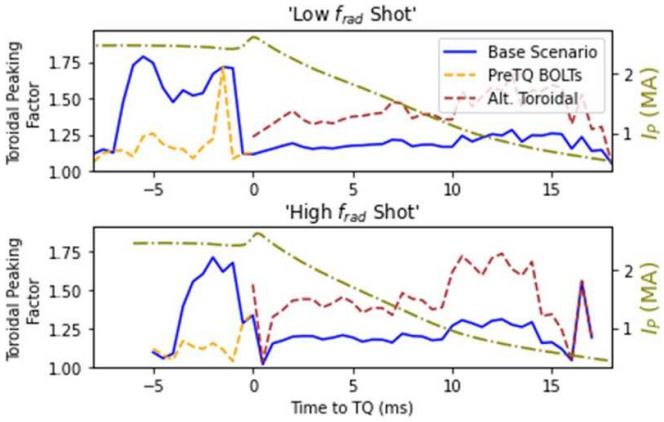

Figure 15. Toroidal peaking factors during the identically prepared 'low' and 'high' f_{rad} disruptions. Emis3D finds significant toroidal peaking at the TQ time on the 'high f_{rad}' shot, and less peaking on the 'low f_{rad}' shot. See text and figures 16 and 17 for description of radiation structures.

toroidal behavior of the best-fit helical structures reveal interesting toroidal transport.

With the pre-TQ M-BOLT structures removed, the best fit radiation structures during the pre-TQ are helical. Best fit structures at the TQ and throughout the CQ are M-BOLTs. The radiation structure evolution chosen by Emis3D with this library for the 'low f_{rad}' shot is shown in figures 16 and 17. In this scenario, ring and M-BOLT structure toroidal distributions are handled as a simple step function, as shown in figure 9. In terms of radiated power, this is equivalent to averaging the amplitudes derived from the two arrays.

f_{rad} is closer between the two shots than suggested by the control room analysis, differing by around $\sim$4% instead of $\sim$11%. The change is the result of lower radiated power at the TQ on the 'high f_{rad}' shot. The control room P_{rad} measurement at this time is high, more than double that of the 'low f_{rad}' shot. With Emis3D, we see that the high P_{rad} is likely a measurement error related to toroidal peaking. The best fit radiation structure at this time (figure 18) on the 'high f_{rad}' discharge is peaked, with a TPF of 1.33 (representing $\sim$2$\times$ higher amplitude in one array than the other), and the peak is near the vertical bolometer array. The control room P_{rad} measurement uses only information from the vertical array, and does not consider the lower amplitude of the radiation structure elsewhere in the tokamak (e.g. at the horizontal array location). By using a best-fit structure that accounts for this peaking, Emis3D finds a lower peak P_{rad} on the 'high f_{rad}' discharge, more similar to that of the 'low f_{rad}' shot.

f_{rad} has also increased relative to the control room result for both shots, from 0.8 $\rightarrow$ 0.98 and 0.9 $\rightarrow$ 1.01 respectively, bringing both shots into the ITER definition of fully mitigated. The change in f_{rad} is due to increased P_{rad} during the early to middle CQ on both shots, and may also be the result of previously unaccounted for toroidal peaking. Peaking is low during the CQ compared to the pre-TQ, but not completely negligible. The best fit radiation structures throughout the CQs of both shots are peaked near the horizontal array (figure 19), which implies an underestimate of P_{rad} in the control room analysis, and Emis3D finds higher P_{rad} than the control room result. Note, however, that the lower error bounds for the CQ P_{rad} are large, as other M-BOLT or helical radiation structures with lower radiated power are decent fits to the bolometry data as well.

The shape of the radiation structures in the pre-TQ exhibit interesting toroidal transport that has been observed in simulation. The best fit helical radiation structures in the pre-TQ are shown in figure 16:1–2. At early times, these structures show an expected radiation peak at a point near the injector location, with spreading along the field line through that point. However, the spreading is much greater in the direction of the high-field side. This behavior is consistent with early pre-TQ fast camera images from the deuterium injection discharge shown in figure 1 and with JOREK simulations in section 7, and with the 'magnetic nozzle effect' described in [32].

6.2. Alternate M-BOLT toroidal distribution scenario

Our analysis up to this point treats the toroidal distribution of M-BOLT radiation structures as a simple step function. In this section, we treat M-BOLT structures in the CQ with a sine curve toroidal distribution (figure 9), with one extremum (either a peak or trough) fixed to the injector location. P_{rad} for this case is plotted in figure 20. In this scenario, f_{rad} is lower than in the base scenario, and toroidal peaking factors are higher throughout the CQ of both shots. The 'high f_{rad}' shot has significantly higher peaking at the TQ than the 'low f_{rad}' shot in this scenario as well as the base scenario, although the resulting P_{rad} adjustment is smaller than in the base scenario.

The alternate scenario is not more physically motivated than the step function case. The sinusoidal distributions explored here are unlikely, as there is a trough at the injector location throughout the CQ, when high impurity concentration

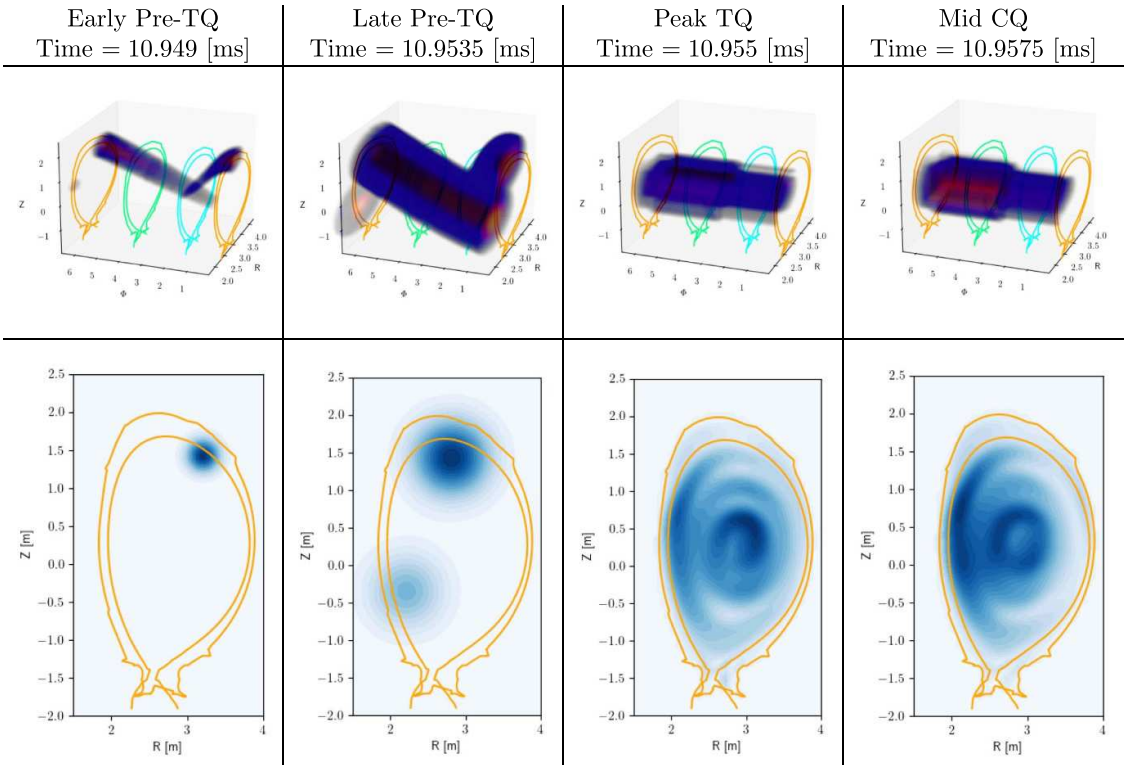

Figure 16. Best fit radiation structures at four characteristic times from the 'low f_{rad}' disruption. The first wall contour and last closed flux surface are plotted in orange at the toroidal location of the injector. The green curves are at the location of the horizontal bolometer array, and the light blue curves at the location of the vertical array. Helical radiation structures are the best fits for the pre-TQ. In the early pre-TQ, thin helicals with small gaussian cross-sections are the best fits, while wider helicals are preferred later in the pre-TQ. M-BOLT radiation structures tailored to the TQ and CQ, with some toroidal peaking away from the injector location, are best fits for the thermal and current quench. Differences in local emissivity are magnified in plots of M-BOLT radiation structures to make toroidal peaking visible.

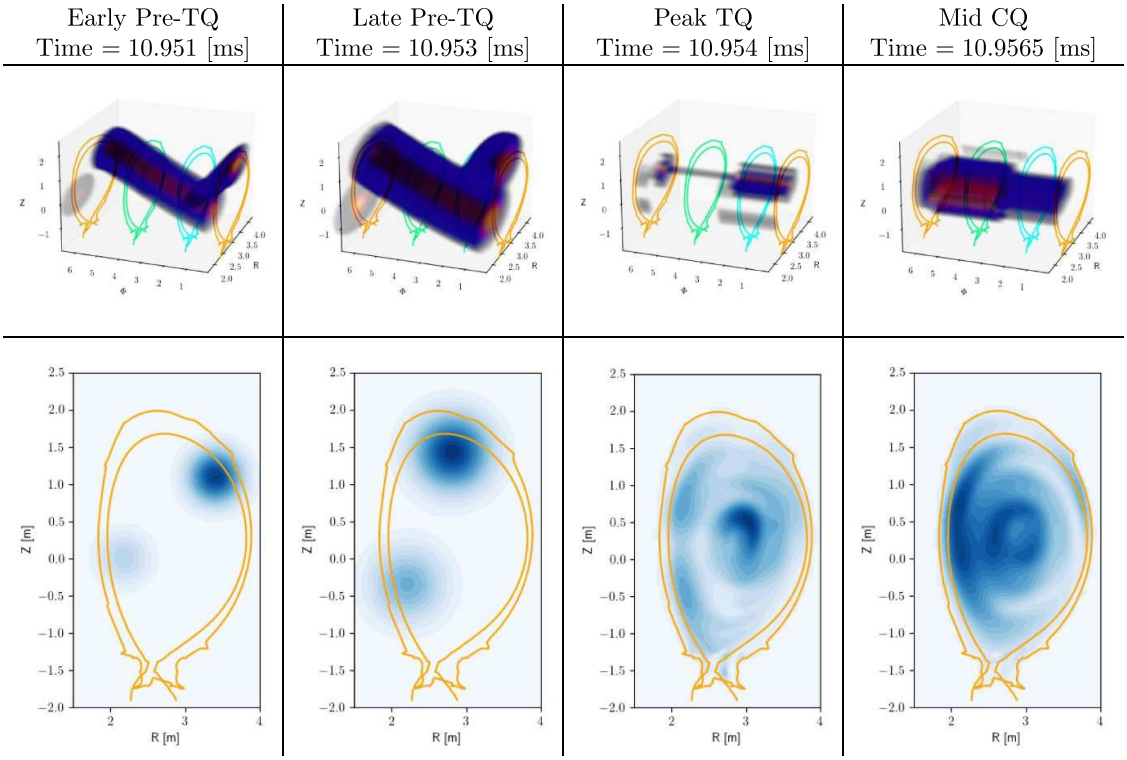

Figure 17. Best fit radiation structures at four characteristic times from the 'high f_{rad}' disruption. Generally similar trends to the 'low f_{rad} disruption are observed. The 'high f_{rad}' shot has a shorter pre-TQ, with only around two milliseconds between the first and last clear helical structures instead of the around five milliseconds on the 'low f_{rad}' shot. Differences in local emissivity are magnified in plots of M-BOLT radiation structures to make toroidal peaking visible.

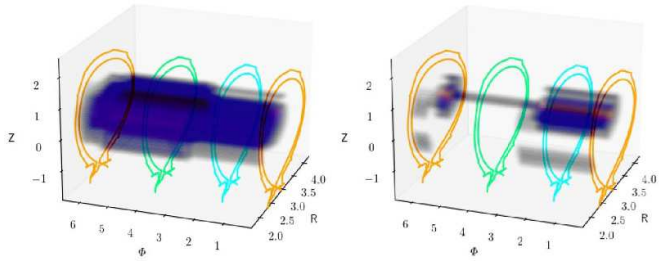

Figure 18. The best fit radiation structure at the thermal quench peak on the 'low f_{rad}' (left) and 'high f_{rad}' (right) disruptions. The high f_{rad} structure is strongly peaked in the region visible to the vertical bolometer array (light blue), causing an overestimate of P_{rad} in the control room analysis, while the low f_{rad} structure is slightly peaked away from the vertical bolometer array, and is not overestimated in the control room analysis.

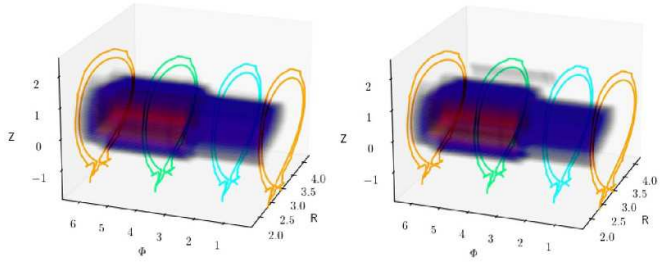

Figure 19. Best fit radiation structures from the current quench of the 'low f_{rad}' (left) and 'high f_{rad}' (right) disruptions. Both best fit structures are M-BOLT structures from their respective shots. Both structures are moderately peaked away from the vertical bolometer array, suggesting an underestimate of radiated power in the current quench in the control room analysis.

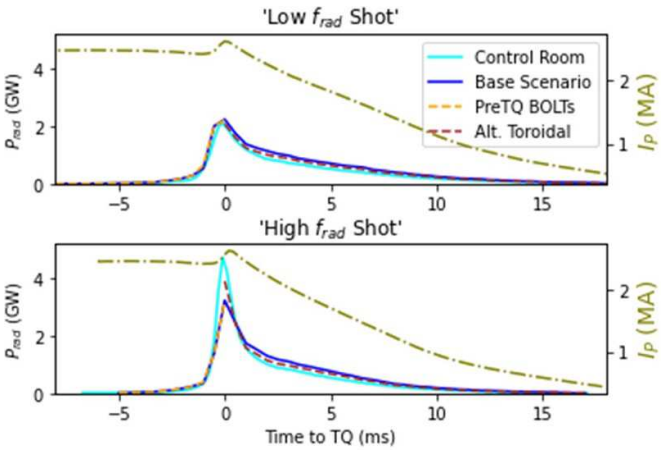

Figure 20. Comparison of best fit P_{rad} values in various physical models. In 'PreTQ BOLTs', M-BOLT radiation structures from the pre-TQ of each discharge are included in the radiation structure library. In 'Alt. Toroidal', the toroidal distribution of current quench M-BOLT structures is treated sinusoidally rather than linearly.

near the injector should cause a peak. This alternate scenario is presented to demonstrate the variation in f_{rad} and TPF that is possible with limited toroidal diagnostic resolution.

6.3. Helical TQ scenario

In section 6.1, M-BOLTs are suppressed in favor of helical structures in the pre-TQ, based on the evidence presented in section 5. M-BOLTs are not suppressed in favor of helicals in the TQ, as we do not have experimental evidence of single field line helical structures in the TQ, and radiation structures approaching the TQ seen in JOREK simulations are more similar to BOLT inversions than to single field line helicals. However, the TQ is less easily observed and modeled than either the pre-TQ or the CQ, and the true TQ radiation structure could be very different from both M-BOLTs and single helicals. A more accurate description of TQ radiation will likely require future work and new additions to the radiation structure library. However, we can gather some insight to the true TQ radiation behavior by comparing the best fit radiation structures in each of the three categories currently available in Emis3D. The TQ radiated power and TPF for each of these cases are reported in figure 21.

Similar peak P_{rad} is found with the best fit TQ helicals as with M-BOLTs. The difference in peak P_{rad} between the two discharges is much smaller than predicted by the weighted average, at $\sim$1.3 GW instead of of $\sim$2.6 GW. However, the toroidal peaking is not higher on the 'high f_{rad}' discharge than on the 'low f_{rad}' discharge. In this case, the diminished peak P_{rad} gap is a more complicated effect of the helical structure, and of overall lower peak P_{rad} on both discharges. It may also be relevant that the Emis3D helical structure is constrained to peak at the toroidal angle of the gas injection. As in the previous section, toroidal peaking factors vary significantly with different physical assumptions, but the diminished peak P_{rad} gap appears to be a more robust result.

The reduced χ^2_r of even the best fit ring structure at the TQ is very high on both discharges, more than twice that of the best helical and M-BOLT, and the corresponding P-value and goodness of fit are very poor. The very low P_{rad} found in this case should not be taken seriously. However, there is a similar disparity in toroidal peaking factors on the two discharges to that found with the best fit M-BOLTs. This suggests that the toroidal peaking found with the M-BOLTs is not an artifact of the specific best fit BOLT inversion, and would be a recurring result with other nominally toroidally self-similar radiation structures.

6.4. Single-channel bolometer results

The single-channel bolometers are noisy on the timescale used for reconstructions, and are not used in our main fitting process. The average brightness over an entire disruption is more reliable, and can be compared to synthetic values, as a post-fitting check of the results. Single-channel bolometer brightnesses are not absolutely calibrated due to hardware limitations. However, all four channels have the same poloidal sightline into the plasma, so the relative brightness of each channel can be compared. The single-channel bolometer relative calibrations found in [12] are used here.

In experiment, the single-channel bolometer closest to the injection location ('channel 1'), receives two or more times

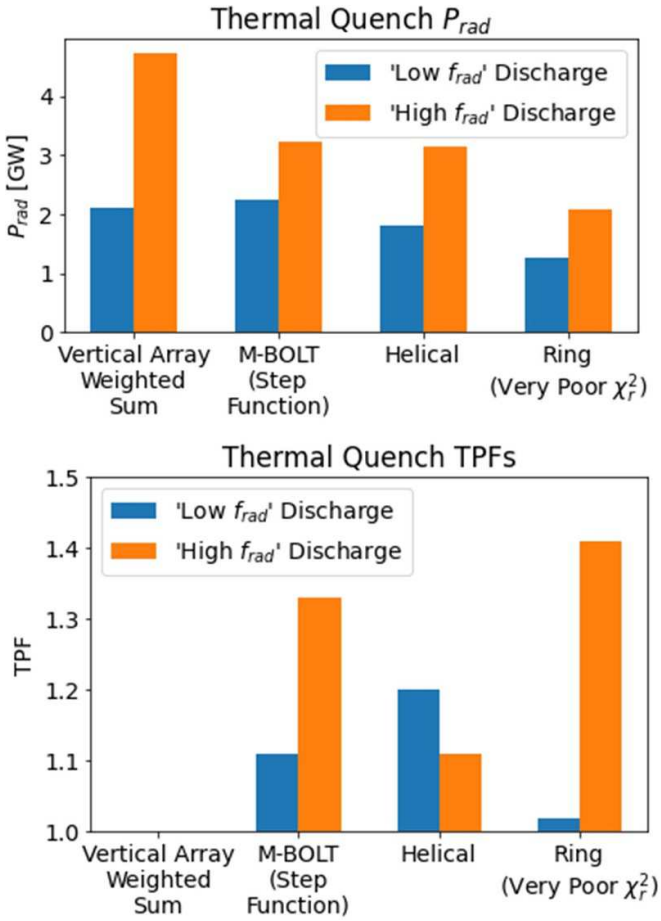

Figure 21. P_{rad} and toroidal peaking factor at the thermal quench using the best fit from each category of radiation structure. The M-BOLT values are referenced in section 6.1, while the Helical values are referred to in section 6.3.

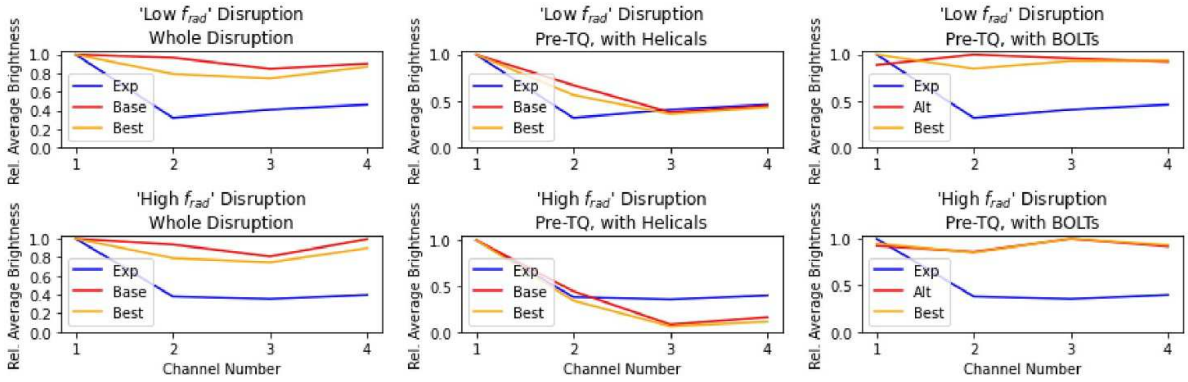

Figure 22. Averaged single bolometer channel brightnesses, normalized to the brightest channel. In the experimental results shown in blue, the average brightness of channel 1 over the entire disruption is more than twice that of the other three channels. This result is not matched in the average synthetic channel brightnesses from the whole-disruption base scenario (left). The higher channel 1 brightness is somewhat captured when averaging synthetic brightnesses over only the pre-TQ in the base scenario (middle), where helical radiation structures are the best fits.

the integrated brightness of any of the other three channels (channels 2–4), on both the 'high' and 'low f_{rad}' discharges. This result is not well reproduced by Emis3D in our base scenario, which finds roughly equal brightnesses for all four channels, as seen in figure 22. A 'best case' scenario, where a radiation structure is chosen from the two-standard-error uncertainty pool with the highest channel 1 signal relative to the other three, is similarly unable to produce this result. However, in the pre-TQ alone, best-fit helical structures exhibit much higher channel 1 brightness than channels 2–4, as seen in both figures 22 and 23. This is the only case where the experimental single-channel bolometer brightness

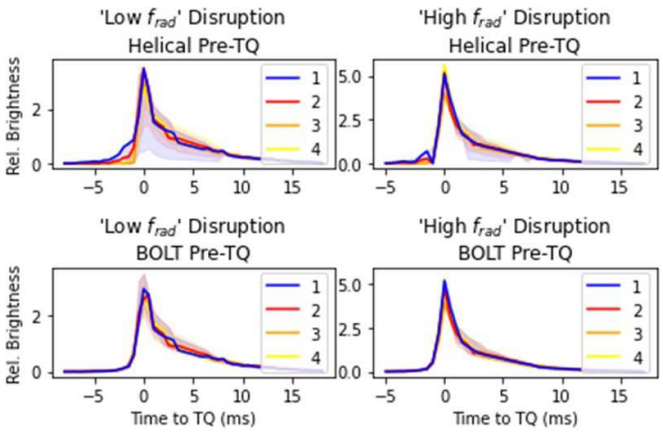

Figure 23. Time series of synthetic single-channel bolometer brightnesses produced using the best-fit radiation structures from the base scenario (top), and in the alternate scenario where pre-TQ M-BOLTs are included in the radiation structure library (bottom). In the base scenario pre-TQ, channel 1 receives significantly higher brightness than the other three channels, as also shown in figure 22.

ratios are successfully reproduced, which provides additional support for the choice of helical structures in the pre-TQ. The failure to reproduce the whole-disruption result may be due to a lack of toroidally asymmetric structures in the radiation structure library tailored to the TQ. Best-fit helical structures during the TQ do not produce relatively high channel 1 brightnesses as they do in the pre-TQ.

7. JOREK Comparison

Emis3D can also be used to provide feedback for tokamak disruption simulations. 3D MHD simulations are a valuable tool for predicting plasma behavior in regimes that are not accessible to current devices, such as fusion reactor-scale disruptions, as well as to understand the complicated physics in present experiments. A previous simulation study of JET MGI provides a quantitative comparison of the radiated power to experiment and a qualitative comparison of the time evolution of measured brightness using native JOREK synthetic bolometry [33]. Emis3D provides high fidelity synthetic bolometry (and cameras) leveraging Cherab and performs goodness of fit tests on the simulated data. With Emis3D, we can quantitatively compare how well simulated radiation structures match experiment and how they perform relative to a variety of more basic radiation structures. JOREK is a nonlinear extended MHD code for plasma simulation in diverted tokamaks [34, 35]. JOREK simulations can produce time-resolved 3D emissivity distributions for a plasma disruption, which are used as candidate radiation structures.

Here we will compare four simulations of the SPI mitigation scenario corresponding to the pre-TQ of the 'low' and 'high f_{rad}' discharges, each with slight changes to simulation parameters to attempt to improve the fidelity of the simulation [29, 36]. In all four simulations, all pellet shards are assumed to be initially located at the exit of the shatter tube, and then to spread into the plasma according to the their velocity and angular distributions, with a Gaussian shape. A relation is introduced between size and velocity of each shards, so that both fastest and slowest shards are small, while the shards with velocities close to average (located in the bulk of the SPI plume) are of all sizes. This dependence between shard sizes and velocities is chosen to reproduce laboratory observations showing that typically the middle of the plume carries $\sim$75% of the fragments and $\sim$99% of the solid mass [37].

Each successive simulation is intended to more closely match the experimental SPI plume than the previous simulation, with simulation 4 providing the most realistic description. From simulation 1 to simulation 2, the toroidal extent of impurity sources representing injected pellet shards is decreased, from one radian to one half radian. In this way, the unrealistically toroidally elongated shape of the ablation cloud of each pellet shard in simulation 1 is reduced to the resolution limit allowed by the employed toroidal Fourier harmonics (up to $n = 10$). From simulation 2 to simulation 3, the velocity spread of pellet shards is increased, from $\pm$25% of the average velocity to $\pm$50%. From simulation 3 to simulation 4, the average velocity of pellet shards is decreased from 200 to 155 m s^{-1} in order to match the experimental pellet velocity determined from the time of flight from the microwave cavity diagnostics to the entrance in the plasma observed by the fast camera diagnostic [20]. As a consequence of the change in the pellet velocity, the number of pellet shards computed using the statistical fragmentation model [38] is reduced from 111 to 32. The average velocity spread is also slightly reduced to $\pm$40%.

We find that all four JOREK simulations show qualitatively similar evolution of radiation structures to the best fit helical structures chosen by Emis3D during the pre-TQ. In the early pre-TQ, JOREK-derived radiation structures show similar helical flux tubes and magnetic nozzle effect behavior to that seen in best fit helical structures, as shown in figure 24. On the 'low f_{rad}' shot, simulations 3 and 4 are equal or better fits to the early pre-TQ radiation structure than basic helical structures. At later pre-TQ times, the JOREK radiation structures broaden out both poloidally and toroidally in a similar manner to the helical best fits, and approach a roughly toroidally symmetric structure at the TQ, similar to the the best fit M-BOLT structure for the 'low f_{rad}' disruption (figure 25). Individual channel brightnesses are shown in figure 26, and show similarity

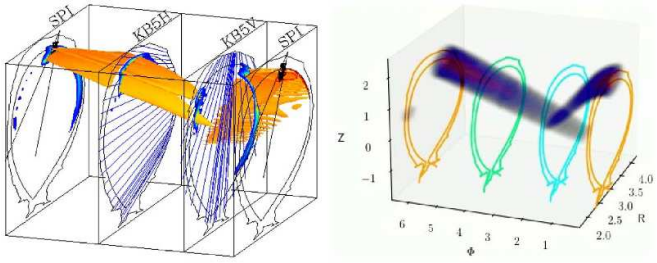

Figure 24. Left: A radiation structure from the early pre-TQ of JOREK simulation 4, 2.5 ms after injection occurs and 1.2 ms after first significant radiation appears. Right: A best-fit helical structure from the early pre-TQ of the 'low f_{rad}' shot, about 1 ms after radiation from the injected pellet is first visible in fast camera images.

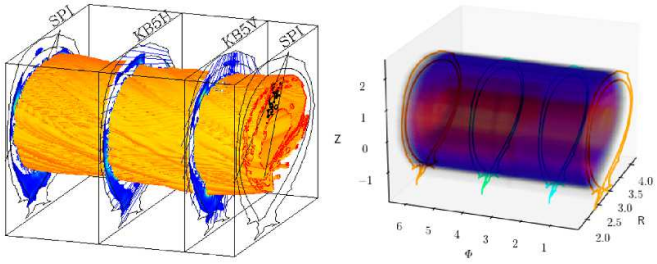

Figure 25. Left: The last radiation structure produced in JOREK simulation 4, just before the thermal quench. Right: the best fit structure at the thermal quench in the base scenario, an M-BOLT. Differences in local emissivity are left un-magnified in this image. For the magnified version, see the 'Peak TQ' structure in figure 16.

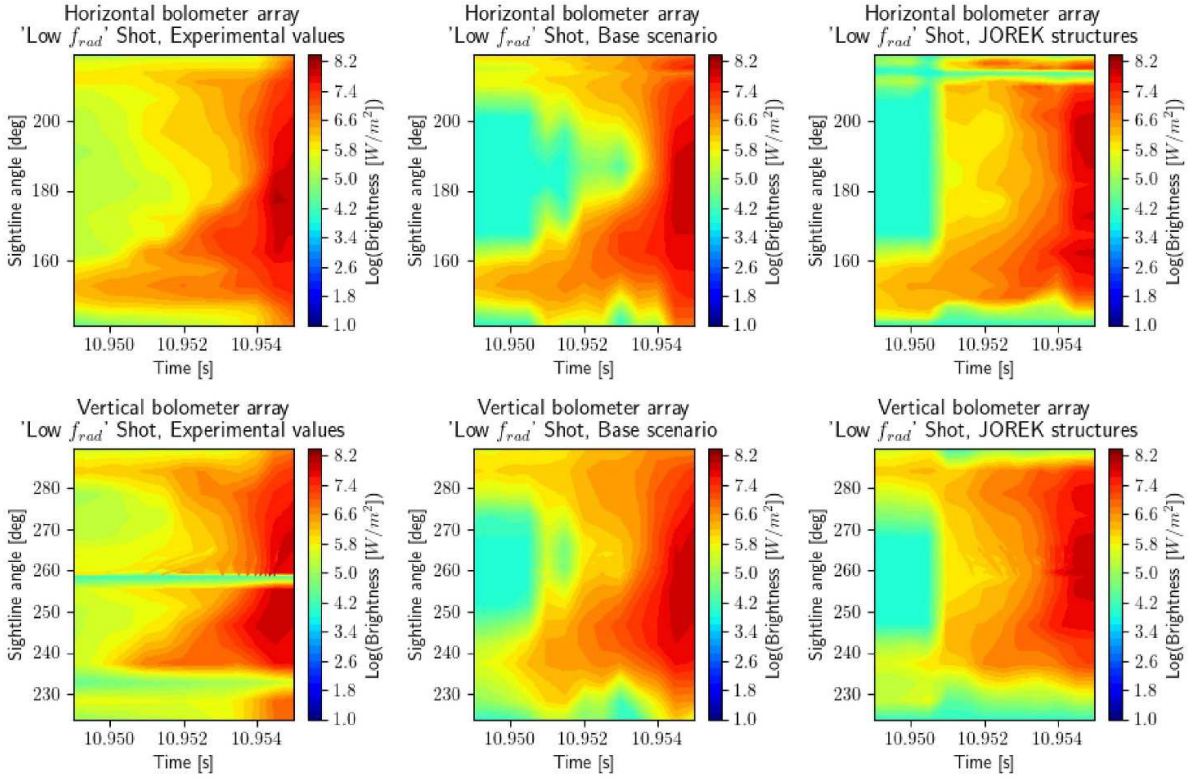

Figure 26. Contour plots of the vertical and horizontal bolometer array channel brightnesses during the pre-TQ of the 'low f_{rad}' disruption, in experiment and with Emis3D. Top: horizontal array, Bottom: vertical array. Left: experimental bolometer brightnesses, Center: base scenario best fit radiation structure synthetic bolometer brightnesses, Right: JOREK simulation 4 best fit radiation structure synthetic bolometer brightnesses. Note that the vertical array channel at angle $\sim 258^{\circ}$ is excluded from the fitting process.

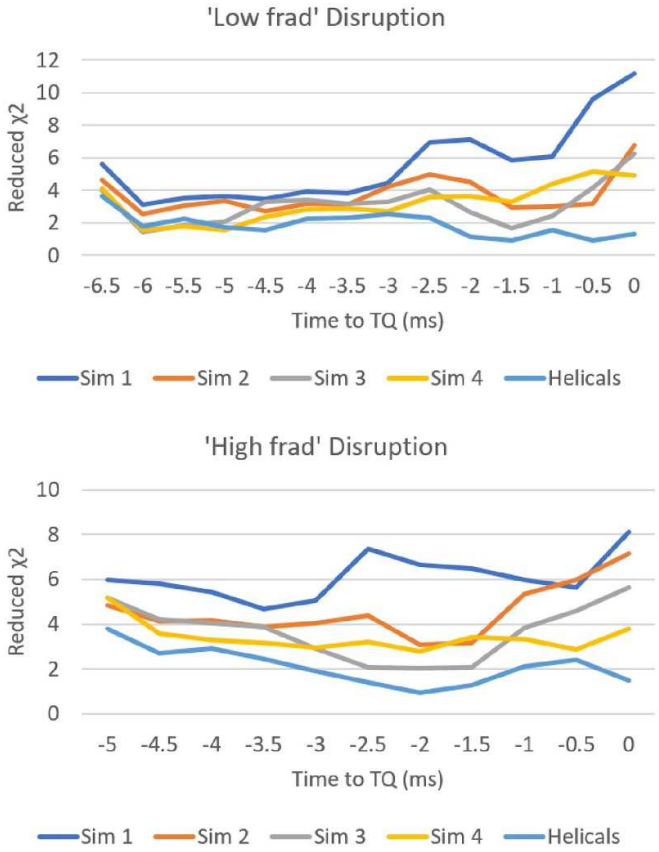

Figure 27. χ^2 plots comparing the quality of fit of the best fit JOREK simulation and helical radiation structures at times during the pre-TQ, for both disruptions. The reduction in best fit χ^2 from simulation 1 to simulation 4 on both discharges demonstrates improved agreement between simulation and experiment.

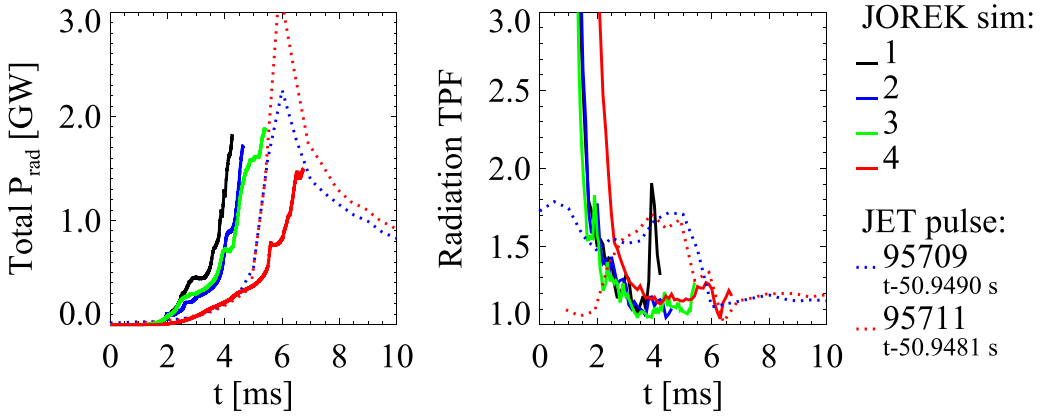

Figure 28. Comparison of P_{rad} and TPF in the four JOREK simulations to those found in the Emis3D base scenario on the 'high f_{rad}' (95 711) and 'low f_{rad}' (95 709) discharges. These JOREK simulations do not include radiation from the initial pre-disruption plasma, so radiation is completely localized at the SPI location and TPF is near infinite until toroidal transport of impurities becomes significant.

between best fit JOREK simulation 4 radiation structures and best fit base scenario radiation structures. We see significant improvement in fits from simulations 1–4 (figure 27), suggesting that the parameter changes in the JOREK simulations succesfully improved their fidelity.

Some challenges for JOREK validation remain. While there is now very good agreement in early pre-TQ P_{rad} between simulation 4 and the Emis3D base scenario (figure 28), there is still disagreement in both P_{rad} and TPF in the later pre-TQ. Further simulation adjustments are being tested to address

these differences. Another validation concern is that the best fitting JOREK structures are not constrained to follow the same time ordering as in the simulation, and in fact they often do not. Structures from later in the simulation are often better fits to earlier times and vice versa. While JOREK simulations qualitatively match broad periods of the pre-TQ, the fine detail may not be an exact match. It is also possoble that that while the viewing geometry of the bolometers is accurately modeled in Emis3D, time smoothing resulting from heat diffusion in the foil and other hardware/software effects on the instrument response are not captured and affect these conclusions.

8. Conclusion

Emis3D has been developed as a feed-forward tomography code for modeling three dimensional radiation structures during disruptions, and has been applied to two SPI-mitigated discharges on JET. Radiation structure characteristics are revealed that are not evident from either weighted-average radiated power analysis or 2D tomographic inversion alone. The 'high f_{rad}' disruption has significantly higher toroidal peaking than the 'low f_{rad}' disruption at the TQ, and accounting for this difference results in more similar f_{rad} values between the two shots. f_{rad} is overall higher on both shots than the control room result due to increased P_{rad} in the CQ.

Radiation structures in the early pre-TQ are consistent with the magnetic nozzle effect. Radiation structure evolution during the pre-TQ is qualitatively consistent with simulations from JOREK. Emis3D is used to confirm improvements in JOREK simulations during the pre-TQ, demonstrated by progressively better reduced χ^2 fits to experimental data.

Questions remain about the root cause of the different peak P_{rad} on each shot. Lower P_{rad} on the 'high f_{rad}' discharge than the control room analysis appears robust across variations in radiation structure assumptions. The total f_{rad} result is found to be sensitive to the functional form of the toroidal distribution.

It is not clear what causes the high TQ TPF on the 'high f_{rad} discharge, but a few hypotheses have emerged. The 'high f_{rad}' disruption had a much shorter pre-TQ stage than the 'low f_{rad}' disruption, which may have hindered toroidal transport of impurities and resulted in an uneven toroidal distribution of radiation. The 'high f_{rad}' disruption may have had stronger MHD activity in the TQ than the 'low f_{rad}' disruption, which could result in a more peaked thermal energy release from the core.

With the capabilities of Emis3D now more fully developed and understood by application to these two discharges, we are ready to address questions concerning the use of SPI and other impurity injection methods for disruption mitigation. We intend to apply Emis3D to a large pool of SPI discharges from the JET 2019 SPI campaign, in particular testing a predicted scaling law between pre-disruption thermal energy fraction and disruption f_{rad} that suggests poor performance of SPI on ITER [7, 31]. This planned study may require additions to the radiation structure pool, such as combinations of helical structures, hollow flux surface annuli, or flux-aligned inversions, to better capture the likely non-axisymmetry of the TQ.

Emis3D is open-source, currently available at https://github.com/bensteinlubrano/Emis3D_Universal, and free to use pending licensing. Certain machine-specific modules are proprietary. A GUI is included and work is ongoing.

Acknowledgments

This work has been carried out within the framework of the EUROfusion Consortium, partially funded by the European Union via the Euratom Research and Training Programme (Grant Agreement No 101052200—EUROfusion). The Swiss contribution to this work has been funded by the Swiss State Secretariat for Education, Research and Innovation (SERI). Views and opinions expressed are however those of the author(s) only and do not necessarily reflect those of the European Union, the European Commission or SERI. Neither the European Union nor the European Commission nor SERI can be held responsible for them.

This material is based upon work supported by the US Department of Energy, Office of Science, Office of Fusion Energy Sciences, under Awards DE-SC0014264. The views and opinions expressed herein do not necessarily reflect those of the Department of Energy.

The JET SPI project is a collaborative effort of EURATOM, the ITER Organization, and the US Department of Energy. It received funding from the ITER Organization. The views and opinions expressed herein do not necessarily reflect those of the of the ITER Organization.

Parts of this work was carried out using the Marconi-Fusion supercomputer.

Appendix

Absolute calibration of radiation structures and correct application of the Cherab code are tested by comparison of Cherab synthetic bolometry data of BOLT-derived radiation structures to experimental bolometry data, here labeled MEasured Line Integrals (MELI). BOLT 2D radiation structures are produced from bolometry data by the JET bolometry team upon request. BOLT structures are optimized to closely fit experimental data, using independently calculated (non-Cherab) synthetic measurements, here labeled Back-Calculated Line Integrals (BCLIs), produced by the standard JET workflow. The BOLT radiation structures are input to the Emis3D workflow, and new synthetic bolometry data for these structures are generated by Cherab. This synthetic bolometry data is then compared to the original experimental bolometry data from which the BOLT structure was derived, and to the BCLIs for that structure, and close agreement is observed, as shown in figure 29. The close agreement validates that the Emis3D-Cherab workflow is accurate and that radiation structures used in Emis3D are absolutely calibrated.

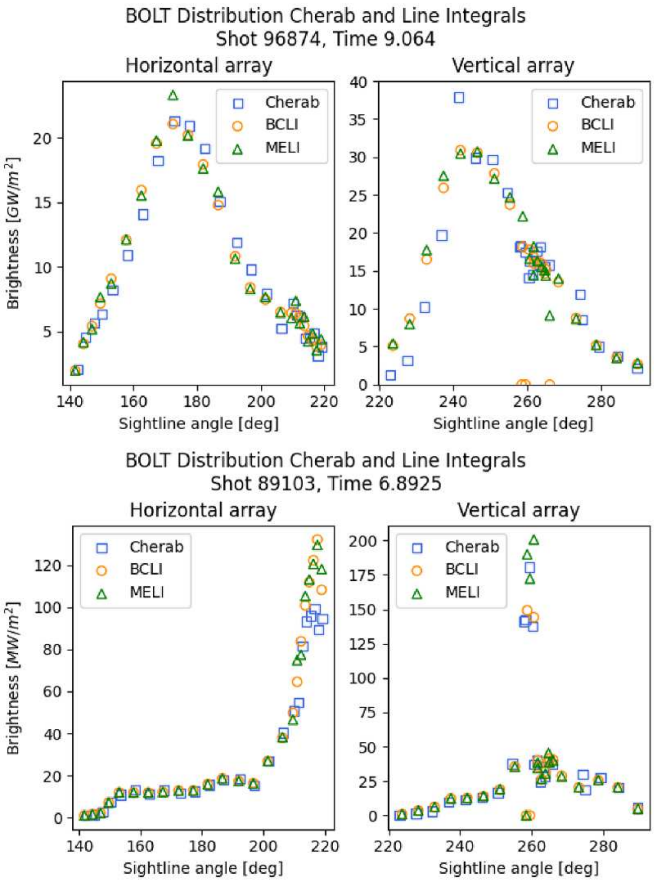

Figure 29. Comparison of Cherab synthetic measurements of a BOLT radiation structure to the experimental measurements from which the BOLT structure is derived, and to JET synthetic measurements of that BOLT structure. Two example shots and times are shown. Top is from the current quench of the deuterium SPI dishcharge. Bottom is from flattop operation of an arbitrarily chosen discharge. The sightline angle is the counterclockwise angle in the poloidal plane between the outward R (major radial) vector and the bolometer sightline vector.

ORCID iDs

B. Stein-Lubrano https://orcid.org/0000-0001-8152-0814
R. Sweeney https://orcid.org/0000-0003-3408-1497
D. Bonfiglio https://orcid.org/0000-0003-2638-317X
J. Lovell https://orcid.org/0000-0001-9565-3466
P. Carvalho https://orcid.org/0000-0002-8480-0499
L. Baylor https://orcid.org/0000-0002-0325-7771
R.S. Granetz https://orcid.org/0000-0002-6560-1881
S. Jachmich https://orcid.org/0000-0001-8289-536X
M. Kong https://orcid.org/0000-0002-2004-3513
M. Lehnen https://orcid.org/0000-0001-6043-8803
C. Maggi https://orcid.org/0000-0001-7208-2613
E. Marmar https://orcid.org/0000-0002-5283-0546
E. Nardon https://orcid.org/0000-0003-0427-2292
P. Puglia https://orcid.org/0000-0003-4125-8465
U. Sheikh https://orcid.org/0000-0001-6207-2489
D. Shiraki https://orcid.org/0000-0002-1452-6949
S. Silburn https://orcid.org/0000-0002-3111-5113

References

[1] Ikeda K. 2007 *Nucl. Fusion* **47** E01
[2] Creely A.J. *et al* 2020 *J. Plasma Phys.* **86** 865860502
[3] Lehnen M., Campbell D., Hu D., Kruezi U., Luce T., Maruyama S., Snipes J. and Sweeney R. 2018 *27th IAEA Fusion Energy Conf.* (available at: https://inis.iaea.org/search/search.aspx?orig_q=RN:50052430)
[4] Hollmann E.M. *et al* 2015 *Phys. Plasmas* **22** 021802
[5] Jachmich S. *et al* 2022 *Nucl. Fusion* **62** 026012
[6] Sweeney R. *et al* 2021 *63rd APS DPP Annual Meeting* https://meetings.aps.org/Meeting/DPP21/Session/JO07.5
[7] Lehnen M. *et al* 2013 *Nucl. Fusion* **53** 093007
[8] Lehnen M. *et al* 2015 *J. Nucl. Mater.* **463** 39–48
[9] Lehnen M. *et al* 2011 *Nucl. Fusion* **51** 123010
[10] Lehnen M., Gerasimov S., Jachmich S., Koslowski H., Kruezi U., Matthews G., Mlynar J., Reux C. and de Vries P. 2015 *Nucl. Fusion* **55** 123027
[11] Sheikh U. *et al* 2021 *Nucl. Fusion* **61** 126043
[12] Lovell J., Reinke M.L., Sheikh U.A., Sweeney R., Puglia P., Carvalho P. and Baylor L. 2021 *Rev. Sci. Instrum.* **92** 23502
[13] Sweeney R., Raman R., Eidietis N., Herfindal J., Hollmann E., Hu D., Lehnen M., Shiraki D. and Snipes J. 2018 *45th EPS Conf. on Plasma Physics* (*Czech Republic*, *2–6 July*) (available at: http://ocs.ciemat.es/EPS2018PAP/pdf/P4.1046.pdf)
[14] Izzo V.A. 2013 *Phys. Plasmas* **20** 056107
[15] Herfindal J.L., Shiraki D., Baylor L.R., Eidietis N.W., Hollmann E.M., Lasnier C.J. and Moyer R.A. 2019 *Nucl. Fusion* **59** 106034
[16] Sweeney R. *et al* 2021 *Nucl. Fusion* **61** 66040
[17] Sweeney R. 2020 *62nd APS DPP Annual Meeting* https://meetings.aps.org/Meeting/DPP20/Session/TI02.4
[18] Stein-Lubrano B. *et al* 2022 *APS DPP Annual Meeting* https://meetings.aps.org/Meeting/DPP22/Session/YO03.3
[19] Angelone M., Pillon M., Marinelli M., Milani E., Prestopino G., Verona C., Verona-Rinati G., Coffey I., Murari A. and Tartoni N. 2010 *Nucl. Instrum. Methods Phys. Res.* A **623** 726–30
[20] Baylor L.R. *et al* (JET Contributors) 2021 *Nucl. Fusion* **61** 8
[21] Stankunas G and Rimini F 2019 Accurate determination of radiated power density profile using bolometer data for dt baseline scenario at jet (available at: https://inis.iaea.org/search/search.aspx?orig_q=RN:53079989)
[22] Carr M., Meakins A., Bernert M., David P., Giroud C., Harrison J., Henderson S., Lipschultz B. and Reimold F. 2018 *Rev. Sci. Instrum.* **89** 083506
[23] Carr M., Lovell J., Tomes M., Neverov V., Meakins A., Munechika K., Stańczak D. and Bold D. 2021 Cherab/core: Release v1.3.0 (available at: https://zenodo.org/record/5778961)
[24] Ingesson L., Alper B., Peterson B.J. and Vallet J.C. 2008 *Fusion Sci. Technol.* **53** 528–76
[25] Mlynar J, Craciunescu T, Ferreira D R, Carvalho P, Ficker O, Grover O, Imrisek M and Svoboda J 2019 *J. Fusion Energ.* **38** 458–66
[26] Ferreira D.R., Carvalho P.J. and Fernandes H. 2020 *IEEE Trans. Plasma Sci.* **48** 36–45
[27] Bevington P. and Robinson D. 2003 *Data Reduction and Error Analysis for the Physical Sciences* 3rd edn (McGraw-Hill)
[28] Kim J., Kim J., Jang J., Kwak S. and Ghim Y. 2022 *64th APS DPP Annual Meeting* https://meetings.aps.org/Meeting/DPP22/Session/PO05.2
[29] Bonfiglio D. *et al* (JOREK Team and JET Contributors) 2022 *48th EPS Conf. on Plasma Physics* http://ocs.ciemat.es/EPS2022PAP/pdf/O3.101.pdf
[30] McClenaghan J. *et al* 2023 *Nucl. Fusion* **63** 066029
[31] Sheikh U. *et al* 2020 *Nucl. Fusion* **60** 126029

[32] Izzo V.A. *et al* 2015 *Nucl. Fusion* **55** 73032
[33] Nardon E. *et al* 2021 *Plasma Phys. Control. Fusion* **63** 115006
[34] Hoelzl M. *et al* 2021 *Nucl. Fusion* **61** 065001
[35] Hu D., Huijsmans G.T.A., Nardon E., Hoelzl M., Lehnen M. and Bonfiglio D. 2021 *Plasma Phys. Control. Fusion* **63** 125003
[36] Bonfiglio D. 2024 Validation of 3d mhd simulations of mixed ne-d2 shattered pellet injection in jet (in preparation)
[37] Gebhart T.E., Baylor L.R. and Meitner S.J. 2020 *Fusion Sci. Technol.* **76** 831–5
[38] Gebhart T.E., Baylor L.R. and Meitner S.J. 2020 *IEEE Trans. Plasma Sci.* **48** 1598–605